ETH zürich

AK-PDEMi: A FAILURE-INFORMED ENRICHMENT ALGORITHM FOR IMPROVING THE AK-PDEM IN RELIABILITY ANALYSIS

Zhou, T. and Marelli, S. and Sudret, B. and Peng, Y.

CHAIR OF RISK, SAFETY AND UNCERTAINTY QUANTIFICATION
STEFANO-FRANSCINI-PLATZ 5
CH-8093 ZÜRICH

Risk, Safety & Uncertainty Quantification

Data Sheet

Journal:	Mechanical Systems and Signal Processing
Report Ref.:	RSUQ-2022-004
Arxiv Ref.:	-
DOI:	-
Date submitted:	10/2021
Date accepted:	09/06/2022

AK-PDEMi: a failure-informed enrichment algorithm for improving the AK-PDEM in reliability analysis

Tong Zhou[a,b], Stefano Marelli[c], Bruno Sudret[c], Yongbo Peng[a,d,**]

[a] State Key Laboratory of Disaster Reduction in Civil Engineering, Tongji University, Shanghai 200092, P. R. China

[b] College of Civil Engineering, Tongji University, Shanghai 200092, P. R. China

[c] Chair of Risk, Safety and Uncertainty Quantification, ETH Zurich, Zurich 8093, Switzerland

[d] Shanghai Institute of Disaster Prevention and Relief, Tongji University, Shanghai 200092, P. R. China

Abstract: A failure-informed enrichment algorithm is devised to improve the performance of the existing adaptive Kriging-probability density evolution method (AK-PDEM) for reliability analysis. This improved method is named the AK-PDEMi. Contrary to empirically prescribing the sample size of representative points in the existing AK-PDEM, the representative point set in the AK-PDEMi is sequentially enriched by new sets of representative points generated by a failure-informed enrichment scheme, which aims to sequentially making fine partitions of the key sub-regions where the representative points make critical contributions to the failure probability. In this regard, a double-loop configuration is devised: the inner loop adaptively refines the accuracy of Kriging model to reduce the Kriging-induced error, and the outer loop involves the failure-informed enrichment process to alleviate the PDEM-associated discretization error. The outer and inner loops are complementary and proceed sequentially until both of their convergence criteria are satisfied. Three numerical examples are studied and comprehensive comparisons are made between the proposed AK-PDEMi and other conventional reliability algorithms. Results show that the AK-PDEMi shows remarkable advantage over the existing AK-PDEM.

Keywords: Failure-informed enrichment; active learning; double-loop configuration; probability density evolution method; Kriging; reliability analysis

1. Introduction

Structural reliability analysis aims at computing the failure probability of engineering systems under various sources of uncertainties [1]. In the past decades, a wide variety of practical reliability methods have been developed and can be classified into four categories [2], i.e., (i) approximation methods; (ii) simulation methods; (iii) numerical integration-based methods; and (iv) active learning-based reliability methods.

Approximation methods consist in approximating the performance function using linear or quadratic Taylor expansion around the most probable point (MPP), e.g., the first-/second-order reliability method (FORM/SORM) [3]. Unfortunately, they may perform poorly when tackling with the problems with strong nonlinearities or multiple MPPs [4]. Simulation methods include the Monte Carlo simulation (MCS) [5] and its advanced variants. The MCS is easy-to-implement and robust, but its computational cost becomes unaffordable in the case of time-consuming computational models, such as finte-element analysis models. Then, several variance reduction

** Corresponding author.

Email addresses: zhoutong@tongji.edu.cn (T. Zhou), marelli@ibk.baug.ethz.ch (S. Marelli), sudret@ethz.ch (B. Sudret) pengyongbo@tongji.edu.cn (Y. Peng)

Preprint submitted to *Mechanical Systems and Signal Processing*.

techniques have been proposed, e.g., the importance sampling (IS) [6] and the subset simulation (SuS) [7]. They attain a remarkable reduction of computational costs, in comparison with the crude MCS. The basic idea of numerical integration-based methods is to derive the probability density function (PDF) of the performance function, thereby the failure probability can be readily computed by a one-dimensional integral of that PDF. They can be further categorized into the method of moments [8] and the probability density evolution method (PDEM) [9]. In the method of moments, the target PDF is approximated by fitting an appropriate probability distribution model under the constraints of its statistical moments of finite orders. Hence, its performance depends on both the versatility of the probability distribution models and the estimation accuracy of the statistical moments [10]. In the PDEM, the target PDF is derived via solving a series of the so-called generalized probability density evolution equations (GDEEs) [11]. This nonparametric manner allows for more flexibility of the PDEM over the method of moments. However, the existing numerical algorithm of the PDEM still suffers from relatively high computational burden [2].

Active learning-based reliability methods [12, 13] aim to reduce the overall computational costs of those above-mentioned reliability methods through the use of metamodels, a.k.a. surrogate models. The metamodels are adaptively refined by adding new computational model evaluations to their experimental designs based on a so-called learning function, and this iterative process is continued until a suitable convergence criterion is satisfied. Hence, the active learning-based framework generally involves four basic modules, namely metamodel, reliability algorithm, learning function and convergence criterion, and are elucidated as follows. (a) Commonly-used metamodels include Kriging [14], polynomial chaos expansion [15] and support vector regression [16]. Different from other types of metamodels, the Kriging not only provides the predicted value at an unknown point, but also the prediction variance. The latter serves as a built-in error measure and facilitates deriving the learning functions. Hence, the Kriging model has gained overwhelming popularity, and the most representative one is the adaptive Kriging-Monte Carlo simulation (AK-MCS) [14]. Furthermore, the multi-level [17] and multi-fidelity metamodels [18] have been explored in the active learning-based scheme. (b) Thanks to the generality of the MCS, it is naturally the most widely-used one in the active learning-based framework, such as the AK-MCS [14]. Further, those variance-reduction techniques are also explored, e.g., the adaptive Kriging with exploration and exploitation-subset simulation (AKEE-SuS) [19] and the adaptive Kriging-importance sampling (AK-IS) [20]. Besides, in view of the promising performance of the PDEM, it has been combined with the Kriging in the active learning-based framework, e.g., the adaptive Kriging-probability density evolution method (AK-PDEM) [2, 21, 22]. (c) Learning functions lie at the core of active learning-based framework and are naturally related to both the reliability algorithms and the metamodel types. With respect to simulation methods, popular Kriging-related learning functions include the expected feasibility function (EFF) [23] and the misclassification-related U function [14]; besides, several learning functions that accommodate to any type of metamodels have been devised, such as the constrained min-max function [24] and the fraction of bootstrap replicates [15]. With respect to the PDEM, a learning function called Taylor expansion-based adaptive design (TEAD) was initially proposed in [2], which aims to ensure the overall accuracy of metamodels on the whole representative point set, so as to secure the accuracy of failure probability; whereas, the harsh difficulty of maintaining the global accuracy of metamodels incurs remarkable computational costs, especially in the complex engineering problems. Then, two Kriging-related learning functions called the PDEM-information entropy (PIE) [21] and the PDEM-oriented expected improvement function (PEIF) [22] were proposed according to the requirement of the PDEM on the local accuracy

of metamodels, and they showed an enhancement of computational efficiency over the TEAD. (d) The convergence criteria generally consist of three types in the existing literature. The first one is defined based on the learning function values, e.g., $\max_{\boldsymbol{x}} \mathrm{EFF}(\boldsymbol{x}) \le 10^{-3}$ in [23] and $\max_{\boldsymbol{x}} U(\boldsymbol{x}) \ge 2$ in [14]. The second one is defined based on the confidence bound of the estimated failure probability, considering the statistical uncertainty of surrogate predictions, such as [22, 25]. The third one is defined according to the stabilization of the failure probability estimates within several consecutive iterations, such as [13, 26].

Basically, there are two main loops in the active learning-based scheme, namely the outer and inner loops. The inner loop aims to ensure sufficient accuracy of metamodels in the key sub-regions, while the outer loop intends to reduce the error associated with the reliability estimation algorithms. The outer and inner loops proceed sequentially until both of their stopping conditions are satisfied. Take the combination of adaptive matemodels and simulation methods for example, the simulation methods in the outer loop is considered to be converged when the coefficient of variation (COV) of the estimated failure probability is lower than a prescribed tolerance, e.g., $\mathrm{COV}_{\hat{P}_f} \le 5\%$ [14]. In this double-loop configuration, the metamodel module in the inner loop and the reliability estimation module in the outer loop are generally complementary. Specifically, the sample set generated by the reliability estimation module in the outer loop serve as the candidate pool for the adaptive refinement of metamodels, and the metamodel produced in the inner loop is employed to assist the computation of failure probability in the reliability estimation module, such as [19, 27]. However, due to lacking the COV-like convergence criterion in the PDEM, the existing AK-PDEM only involves the inner loop, and the sample size of the PDEM-generated representative point set, i.e., the candidate pool, has to be prescribed *a priori*. This implies that, even if sufficient Kriging accuracy is gained by the inner loop, the failure probability estimated by the AK-PDEM still has the risk of deviating from the true one, due to the probable insufficiency of the prescribed representative point set. Hence, a complete double-loop configuration is needed for the AK-PDEM.

To this end, a failure-informed enrichment scheme is developed for improving the existing AK-PDEM. Accordingly, the AK-PDEM is renamed as the AK-PDEMi herein. The remainder of this paper is organized as follows. Section 2 briefly introduces the PDEM and the AK-PDEM. Section 3 elucidates the proposed AK-PDEMi. Three numerical examples are investigated in Section 4 to showcase the performance of the AK-PDEMi; Section 5 provides some concluding remarks.

2. The PDEM and the AK-PDEM

Section 2.1 introduces the theory of the PDEM; Section 2.2 elucidates the region of interest (ROI) for the PDEM; Section 2.3 outlines the existing AK-PDEM, as well as its drawbacks.

2.1 The PDEM

The equation of motion for a multiple-degree-of-freedom structure under dynamic loads can be expressed as [1]

$$\boldsymbol{M}(\boldsymbol{X})\ddot{\boldsymbol{U}}(t)+\boldsymbol{C}(\boldsymbol{X})\dot{\boldsymbol{U}}(t)+\boldsymbol{f}\left(\boldsymbol{U}(t),\dot{\boldsymbol{U}}(t),\boldsymbol{X}\right)=\boldsymbol{F}(\boldsymbol{X},t) \tag{1}$$

where $\boldsymbol{M}$, $\boldsymbol{C}$ and $\boldsymbol{f}$ are the mass matrix, damping matrix and restoring force vector of the structure, respectively; $\ddot{\boldsymbol{U}}(t)$, $\dot{\boldsymbol{U}}(t)$ and $\boldsymbol{U}(t)$ are the acceleration, velocity and displacement vectors of the structure, respectively;

$\boldsymbol{F}(\boldsymbol{X},t)$ denotes the dynamic loads; $\boldsymbol{X}=\{X_1,\ldots,X_d\}$ is a d-dimensional vector of random variables associated with both structural properties and external loads, with the joint PDF $p_{\boldsymbol{X}}(\boldsymbol{x})$. For a well-posed system, the structural response $Y(t)$ exists and depends on $\boldsymbol{X}$, that is,

$$Y(t)=\Psi\left[\boldsymbol{U}(t),\dot{\boldsymbol{U}}(t)\right]=H_Y(\boldsymbol{X},t) \tag{2}$$

where $\Psi(\cdot)$ is the transform operator; $H_Y(\cdot)$ is the deterministic operator.

In the first-passage problems [28], the failure probability P_f is defined as

$$P_f=\Pr\{\exists t\in[0,T],Y(t)\in\boldsymbol{\Omega}_F\} \tag{3}$$

where $\Pr\{\cdot\}$ denotes the probability for short; $\boldsymbol{\Omega}_F$ is the failure domain; $[0,T]$ is the time duration. Then, Eq. (3) is equivalent to

$$P_f=\Pr\{Y_{\text{EEV}}\in\boldsymbol{\Omega}_F\} \tag{4}$$

where

$$Y_{\text{EEV}}=\underset{t\in[0,T]}{\text{ext}}\{Y(t)\}=\underset{t\in[0,T]}{\text{ext}}\{H_Y(\boldsymbol{X},t)\} \tag{5}$$

is the so-called equivalent extreme-value (EEV) [29] of $Y(t)$ within $[0,T]$; $\underset{t\in[0,T]}{\text{ext}}\{\cdot\}$ denotes the equivalent extreme-value operator. For notational clarity, the mapping of $\boldsymbol{X}\in\mathbb{R}^d$ to the scalar EEV $Y_{\text{EEV}}\in\mathbb{R}$ can be generalized as a computational model $\mathcal{M}$ such that

$$Y_{\text{EEV}}=\mathcal{M}(\boldsymbol{X}),\mathcal{M}:\mathbb{R}^d\mapsto\mathbb{R} \tag{6}$$

and the single evaluation of Eq. (6) may involve the time-consuming structural analysis process.

Take a two-sided barrier problem for example, Eq. (3) can be rewritten as $P_f=\Pr\{\exists t\in[0,T],|Y(t)|\geq u_{\text{thr}}\}$, and u_{thr} is a prescribed threshold. Then, Eq. (5) is specified as $Y_{\text{EEV}}=\max_{t\in[0,T]}(|Y(t)|)$ and Eq. (4) can be evaluated via a one-dimensional integral such that

$$P_f=\int_{\boldsymbol{\Omega}_F}p_{Y_{\text{EEV}}}(y)dy=\int_{u_{\text{thr}}}^{+\infty}p_{Y_{\text{EEV}}}(y)dy \tag{7}$$

where $p_{Y_{\text{EEV}}}(y)$ is the PDF of Y_{EEV}. Clearly, once the $p_{Y_{\text{EEV}}}(y)$ is available, the original reliability assessment in Eq. (3) reduces to a one-dimensional integral in Eq. (7), and the task becomes how to derive the $p_{Y_{\text{EEV}}}(y)$ with desired accuracy and efficiency.

To this end, a virtual stochastic process $V(\tau)$, associated with both the Y_{EEV} and a virtual time parameter τ, needs to be constructed in the PDEM. The typical form of $V(\tau)$ is given as [29]

$$V(\tau)=Y_{\text{EEV}}\cdot\sin\left(\frac{5\pi}{2}\times\tau\right),\ \tau\in[0,1] \tag{8}$$

where $V(\tau)|_{\tau=0}=Y_{\text{EEV}}\cdot\sin\left(\frac{5}{2}\pi\times0\right)=0$ and $V(\tau)|_{\tau=1}=Y_{\text{EEV}}\cdot\sin\left(\frac{5}{2}\pi\times1\right)=Y_{\text{EEV}}$. Eq. (8) shows that the Y_{EEV} is equal to the value of $V(\tau)$ at the time instant $\tau=1$. Hence, the target PDF $p_{Y_{\text{EEV}}}(y)$ equals the evolutionary

PDF of $V(\tau)$, denoted by $p_V(v,\tau)$, at $\tau = 1$, that is,

$$p_{Y_{\text{EEV}}}(y) = p_V(v,\tau)\big|_{v=y,\tau=1} \tag{9}$$

Then, the P_f can be readily evaluated by Eq. (7).

Clearly, the crux of the PDEM lies in deriving the evolutionary PDF $p_V(v,\tau)$ of $V(\tau)$ via solving the GDEE. The corresponding numerical algorithm is shown in Fig. 1 and involves the following four main steps.

Algorithm 1:

(1) **Partition of probability space.** Generate the representative point set $\mathcal{X}_{\text{RP}} = \left\{\boldsymbol{x}^{(1)},\ldots,\boldsymbol{x}^{(N_{\text{RP}})}\right\}$ of size N_{RP} using the GF discrepancy-based strategy [30] (Appendix A) and compute its assigned probabilities $\mathcal{P}_{\text{RP}} = \left\{p_{\text{assign}}^{(1)},\ldots,p_{\text{assign}}^{(N_{\text{RP}})}\right\}$ according to the following expression

$$p_{\text{assign}}^{(j)} = \int_{\boldsymbol{\Omega}^{(j)}} p_{\boldsymbol{X}}(\boldsymbol{x})d\boldsymbol{x},\ j = 1,\ldots,N_{\text{RP}} \tag{10}$$

where $\sum_{j=1}^{N_{\text{RP}}} p_{\text{assign}}^{(j)} = 1$; $\boldsymbol{\Omega}^{(j)}$ denotes the representative volume of $\boldsymbol{x}^{(j)} \in \mathcal{X}_{\text{RP}}$ and can be defined by the Voronoi cell such that [31]

$$\boldsymbol{\Omega}^{(j)} = \left\{\boldsymbol{x} \in \mathbb{R}^d : \left\|\boldsymbol{x}-\boldsymbol{x}^{(j)}\right\| \le \left\|\boldsymbol{x}-\boldsymbol{x}^{(k)}\right\|, \forall \boldsymbol{x}^{(k)} \in \mathcal{X}_{\text{RP}}, j \ne k\right\} \tag{11}$$

where $\boldsymbol{\Omega}^{(i)} \bigcap \boldsymbol{\Omega}^{(j)} = \varnothing, i \ne j$, and $\bigcup_{j=1}^{N_{\text{RP}}} \boldsymbol{\Omega}^{(j)} = \boldsymbol{\Omega}_{\boldsymbol{X}}$. Clearly, the assigned probability $p_{\text{assign}}^{(j)}$ corresponds to the probability over the Voronoi cell of $\boldsymbol{x}^{(j)}$ and can be numerically calculated via the MCS.

(2) **Computational model analyses.** Evaluate the computational model (Eq. (7)) on each $\boldsymbol{x}^{(j)} \in \mathcal{X}_{\text{RP}}$ to obtain the corresponding EEV $y_{\text{EEV}}^{(j)}$, giving rise to $\mathcal{Y}_{\text{RP}} = \left\{y_{\text{EEV}}^{(1)} = \mathcal{M}\left(\boldsymbol{x}^{(1)}\right),\ldots,y_{\text{EEV}}^{(N_{\text{RP}})} = \mathcal{M}\left(\boldsymbol{x}^{(N_{\text{RP}})}\right)\right\}$.

(3) **Solving GDEEs.** For each $\boldsymbol{x}^{(j)} \in \mathcal{X}_{\text{RP}}$, the discretized form of the GDEE is expressed as

$$\frac{\partial p_V^{(j)}(v,\tau)}{\partial \tau} + \dot{V}\left(\boldsymbol{x}^{(j)},\tau\right)\frac{\partial p_V^{(j)}(v,\tau)}{\partial v} = 0,\ j = 1,\ldots,N_{\text{RP}} \tag{12}$$

where $p_V^{(j)}(v,\tau) = \int_{\boldsymbol{\Omega}^{(j)}} p_{V\boldsymbol{X}}(v,\boldsymbol{x},\tau)d\boldsymbol{x}$ is called the j-th partial evolutionary PDF of $V(\tau)$ associated with the $\boldsymbol{x}^{(j)}$; $p_{V\boldsymbol{X}}(v,\boldsymbol{x},\tau)$ is the joint PDF of $\left[V(\tau),\boldsymbol{X}\right]$; $\boldsymbol{\Omega}^{(j)}$ is the Voronoi cell of $\boldsymbol{x}^{(j)}$, see Eq. (11); $\dot{V}\left(\boldsymbol{x}^{(j)},\tau\right)$ is the derivative of $V(\tau)$ with respect to the virtual time τ; see Eq. (8). Then, the initial condition of Eq. (12) is given as

$$p_V^{(j)}(v,\tau)\big|_{\tau=0} = \delta(v)\,p_{\text{assign}}^{(j)},\ j = 1,\ldots,N_{\text{RP}} \tag{13}$$

where $\delta(\cdot)$ is the Dirac's delta function. Solve Eq. (12) under Eq. (13) via the finite difference method [1], resulting in the numerical solution of $p_V^{(j)}(v,\tau),\ j = 1,\ldots,N_{\text{RP}}$.

(4) **Computation of failure probability.** The evolutionary PDF $p_V(v,\tau)$ is calculated as

$$p_V(v,\tau)=\sum_{j=1}^{N_{\mathrm{RP}}} p_V^{(j)}(v,\tau) \tag{14}$$

then, substituting Eq. (14) into Eq. (9), the target PDF $p_{Y_{\mathrm{EEV}}}(y)$ becomes

$$p_{Y_{\mathrm{EEV}}}(y)=\left(\sum_{j=1}^{N_{\mathrm{RP}}} p_V^{(j)}(v,\tau)\right)\Big|_{v=y,\tau=1}=\sum_{j=1}^{N_{\mathrm{RP}}}\left(p_V^{(j)}(v,\tau)\Big|_{v=y,\tau=1}\right)=\sum_{j=1}^{N_{\mathrm{RP}}} p_{Y_{\mathrm{EEV}}}^{(j)}(y) \tag{15}$$

where $p_{Y_{\mathrm{EEV}}}^{(j)}(y)=p_V^{(j)}(v,\tau)\big|_{v=y,\tau=1}$ is called the j-th partial PDF of Y_{EEV} associated with the $\boldsymbol{x}^{(j)}$. Besides, according to the definition of the assigned probability in Eq. (10), the partial PDF $p_{Y_{\mathrm{EEV}}}^{(j)}(y)$ in Eq. (15) has the following property

$$\int_{-\infty}^{+\infty} p_{Y_{\mathrm{EEV}}}^{(j)}(y)dy=\int_{-\infty}^{+\infty}\left(p_V^{(j)}(v,\tau)\Big|_{v=y,\tau=1}\right)dy=\int_{-\infty}^{+\infty}\int_{\boldsymbol{\Omega}^{(j)}} p_{V\boldsymbol{X}}(v,\boldsymbol{x},\tau=1)d\boldsymbol{x}dv=\int_{\boldsymbol{\Omega}^{(j)}} p_{\boldsymbol{X}}(\boldsymbol{x})d\boldsymbol{x}=p_{\mathrm{assign}}^{(j)} \tag{16}$$

which implies that, for each representative point $\boldsymbol{x}^{(j)}$, the integral of $p_{Y_{\mathrm{EEV}}}^{(j)}(y)$ over the whole domain is equal to its assigned probability $p_{\mathrm{assign}}^{(j)}$. Further, substituting Eq. (15) into Eq. (7), yields

$$P_f^{\mathrm{PDEM}}=\int_{u_{\mathrm{thr}}}^{+\infty}\left(\sum_{j=1}^{N_{\mathrm{RP}}} p_{Y_{\mathrm{EEV}}}^{(j)}(y)\right)dy=\sum_{j=1}^{N_{\mathrm{RP}}}\left(\int_{u_{\mathrm{thr}}}^{+\infty} p_{Y_{\mathrm{EEV}}}^{(j)}(y)dy\right)=\sum_{j=1}^{N_{\mathrm{RP}}} P_f^{(j)} \tag{17}$$

where $P_f^{(j)}=\int_{u_{\mathrm{thr}}}^{+\infty} p_{Y_{\mathrm{EEV}}}^{(j)}(y)dy$ denotes the failure probability incurred by the $\boldsymbol{x}^{(j)}$. Hence, the P_f^{PDEM} is the sum of $P_f^{(j)}, j=1,\ldots,N_{\mathrm{RP}}$.

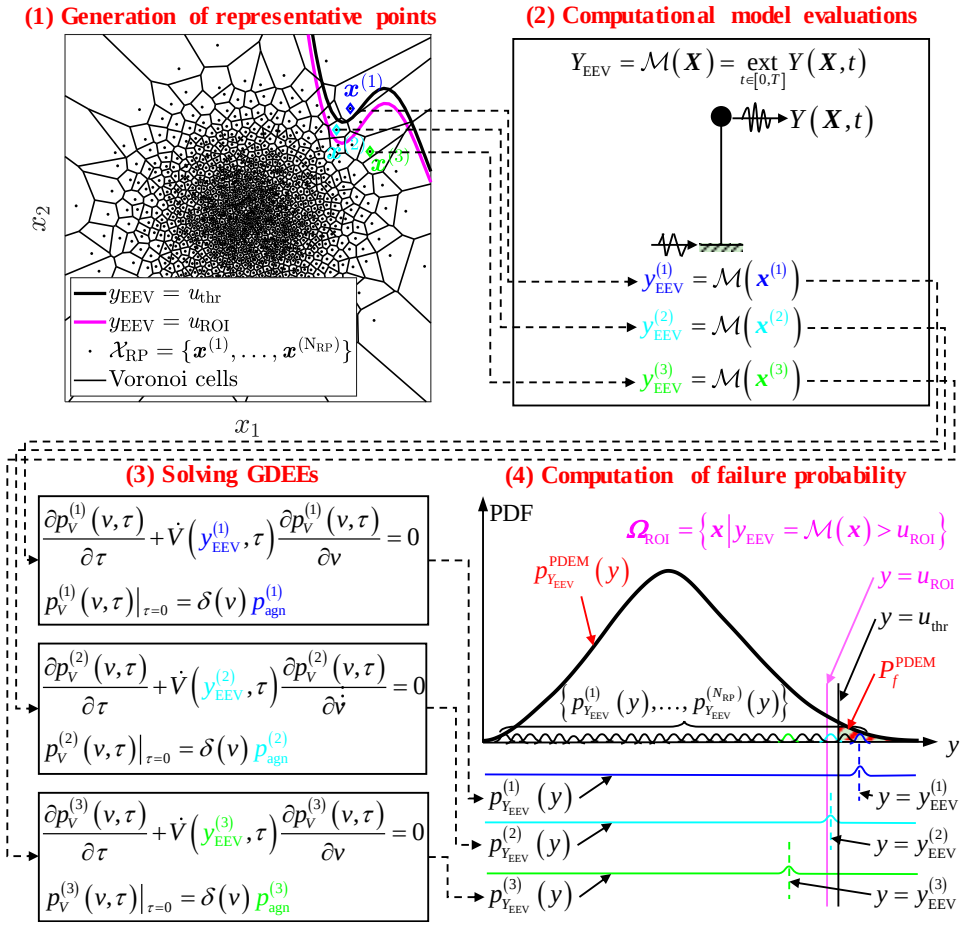

Fig.1 Schematic of the four-step flowchart of the PDEM

Among the four main steps in Fig. 1, Step (2) involves N_{RP} runs of deterministic structural analyses and accounts for the majority of computational burden of the PDEM. To alleviate this, the AK-PDEM was proposed in [21]. As the essential prerequisite of the AK-PDEM, the notation of region of interest (ROI) for the PDEM will be introduced in the next section.

Remark 1: In comparison with those simulation methods, the PDEM involves two particular steps, that is, computing the assigned probabilities in Step (1) and solving the GDEEs in Step (3), as shown in Fig. 1. The samples in simulation methods are drawn from some specific statistical distributions and techniques, e.g., the joint PDF in the MCS or the Markov Chain Monte Carlo (MCMC) in the SuS. By contrast, the PDEM partitions the whole probability space into a series of mutually exclusive and collectively exhaustive subdomains, i.e., the Voronoi cells in Fig. 1; then, the representative points $\boldsymbol{\mathcal{X}}_{\mathrm{RP}}$ actually aim to characterize the probabilistic information associated with their corresponding Voronoi cells and are equipped with the assigned probabilities $\boldsymbol{\mathcal{P}}_{\mathrm{RP}}$. In this regard, the GDEE can be discretized based on the $\boldsymbol{\mathcal{X}}_{\mathrm{RP}}$ accordingly; see Eqs. (12) and (13). Hence, the $\boldsymbol{\mathcal{X}}_{\mathrm{RP}}$ are endowed with more probabilistic information than those statistical samples in simulation methods.

2.2 The region of interest (ROI) for the PDEM

In Fig. 1, the trajectories of three typical representative points among the $\boldsymbol{\mathcal{X}}_{\mathrm{RP}}$, i.e., the $\boldsymbol{x}^{(1)}$, $\boldsymbol{x}^{(2)}$ and $\boldsymbol{x}^{(3)}$, are colored in blue, cyan and green, respectively. For each $\boldsymbol{x}^{(j)} \in \boldsymbol{\mathcal{X}}_{\mathrm{RP}}$, the partial PDF $p_{Y_{\mathrm{EEV}}}^{(j)}(y)$ is centered at the vertical axis of $y = y_{\mathrm{EEV}}^{(j)}$ and decays quickly with the distance to that axis; that is, the specific value of $y_{\mathrm{EEV}}^{(j)}$ dominates the main body of $p_{Y_{\mathrm{EEV}}}^{(j)}(y)$. Hence, according to the locations of different representative points, the whole parameter space can be divided as follows. (i) The first sub-region is covered by these representative points whose EEVs are greater than the threshold u_{thr}, e.g., the blue point $\boldsymbol{x}^{(1)}$ in Fig. 1. The main body of $p_{Y_{\mathrm{EEV}}}^{(1)}(y)$ lies in the failure domain and $P_f^{(1)} = \int_{u_{\mathrm{thr}}}^{+\infty} p_{Y_{\mathrm{EEV}}}^{(1)}(y)dy \gg 0$. (ii) The second sub-region is covered by these representative points whose EEVs are slightly smaller than the u_{thr}, e.g., the cyan point $\boldsymbol{x}^{(2)}$ in Fig. 1. The main body of $p_{Y_{\mathrm{EEV}}}^{(2)}(y)$ lies partially in the failure domain and $P_f^{(2)} = \int_{u_{\mathrm{thr}}}^{+\infty} p_{Y_{\mathrm{EEV}}}^{(2)}(y)dy$ is mildly greater than 0. (iii) The third sub-region is covered by these representative points whose EEVs are far smaller than the u_{thr}, e.g., the green point $\boldsymbol{x}^{(3)}$ in Fig. 1. The main body of $p_{Y_{\mathrm{EEV}}}^{(3)}(y)$ is far away from the failure domain and $P_f^{(3)} = \int_{u_{\mathrm{thr}}}^{+\infty} p_{Y_{\mathrm{EEV}}}^{(3)}(y)dy \approx 0$.

Hence, the failure probabilities incurred by these representative points in the first and second sub-regions account for the vast majority of the P_f^{PDEM}. These two sub-regions are collectively called the region of interest (ROI) for the PDEM and are expressed as

$$\boldsymbol{\Omega}_{\mathrm{ROI}} = \left\{ \boldsymbol{x} \middle| y_{\mathrm{EEV}} = \mathcal{M}(\boldsymbol{x}) \geq u_{\mathrm{ROI}} \right\} \tag{18}$$

where u_{ROI} is the boundary of the ROI (magenta line in Fig. 1). According to Eqs. (17) and (18), the u_{ROI} can be quantitatively determined by the following expression

$$\frac{\left|\sum_{j=1}^{N_{\mathrm{RP}}} P_f^{(j)} - \sum_{j=1}^{N_{\mathrm{RP}}} P_f^{(j)} \cdot \mathbf{1}_{\boldsymbol{\Omega}_{\mathrm{ROI}}}\left(\boldsymbol{x}^{(j)}\right)\right|}{\sum_{j=1}^{N_{\mathrm{RP}}} P_f^{(j)}} \le \varepsilon_{\mathrm{ROI}} \tag{19}$$

where $\mathbf{1}_{\boldsymbol{\Omega}_{\mathrm{ROI}}}(\boldsymbol{x})$ is the indicator function for the $\boldsymbol{\Omega}_{\mathrm{ROI}}$, and equals 1 if $\boldsymbol{x} \in \boldsymbol{\Omega}_{\mathrm{ROI}}$, otherwise 0; $\varepsilon_{\mathrm{ROI}}$ denotes a minor tolerance, say 10^{-5}. According to Eq. (19), the iterative algorithm for determining the u_{ROI} is provided in Appendix B. Then, Algorithm B1 implies that the value of u_{ROI} is only available when both $\boldsymbol{\mathcal{Y}}_{\mathrm{RP}} = \left\{y_{\mathrm{EEV}}^{(j)}, j = 1, \ldots, N_{\mathrm{RP}}\right\}$ (Eq. (7)) and $\left\{P_f^{(j)}, j = 1, \ldots, N_{\mathrm{RP}}\right\}$ (Eq. (17)) are gained from the PDEM. Hence, the value of u_{ROI} is only a byproduct of the standard PDEM and is totally unknown *a priori*.

Remark 2: As shown in Fig. 1, the ROI defines the sub-region in which the representative points make critical contributions to the failure probability; hence, it is an inherent property of the PDEM. Besides, as shown in Algorithm B1, the determination of u_{ROI} depends on the set of representative points generated by the PDEM.

Remark 3: The similarities and differences between the notation of the ROI for the PDEM and the IS are stated as follows. In the IS, the P_f is reformulated as [6]

$$P_f = \int_{\boldsymbol{\Omega}_X} \mathbf{1}_{\boldsymbol{\Omega}_F}(\boldsymbol{x})\, p_X(\boldsymbol{x}) d\boldsymbol{x} = \int_{\boldsymbol{\Omega}_X} \mathbf{1}_{\boldsymbol{\Omega}_F}(\boldsymbol{x}) \frac{p_X(\boldsymbol{x})}{\Psi(\boldsymbol{x})} \Psi(\boldsymbol{x}) d\boldsymbol{x} = \mathbb{E}_{\Psi}\left[\mathbf{1}_{\boldsymbol{\Omega}_F}(\boldsymbol{X}) \frac{p_X(\boldsymbol{X})}{\Psi(\boldsymbol{X})}\right] \tag{20}$$

where $\mathbf{1}_{\boldsymbol{\Omega}_F}(\boldsymbol{x})$ is the indicator function of the failure domain, which equals 1 if $\boldsymbol{x} \in \boldsymbol{\Omega}_F$, otherwise 0; $\Psi(\boldsymbol{X})$ is the d-dimensional importance distribution; $\mathbb{E}_{\Psi}[\cdot]$ denotes the expectation operator with respect to the Ψ. Then, the P_f in Eq. (20) can be estimated by [6]

$$\hat{P}_f^{\mathrm{IS}} = \frac{1}{N_{\mathrm{IS}}} \sum_{j=1}^{N_{\mathrm{IS}}} \mathbf{1}_{\boldsymbol{\Omega}_F}\left(\boldsymbol{x}^{(j)}\right) \frac{p_X\left(\boldsymbol{x}^{(j)}\right)}{\Psi\left(\boldsymbol{x}^{(j)}\right)} = \sum_{j=1}^{N_{\mathrm{IS}}} P_f^{(j)} \tag{21}$$

where the samples $\boldsymbol{\mathcal{X}}_{\mathrm{IS}} = \left\{\boldsymbol{x}^{(1)}, \ldots, \boldsymbol{x}^{(N_{\mathrm{IS}})}\right\}$ of size N_{IS} are drawn from the Ψ; $P_f^{(j)} = \frac{1}{N_{\mathrm{IS}}} \mathbf{1}_{\boldsymbol{\Omega}_F}\left(\boldsymbol{x}^{(j)}\right) \frac{p_X\left(\boldsymbol{x}^{(j)}\right)}{\Psi\left(\boldsymbol{x}^{(j)}\right)}$ denotes the failure probability raised by the $\boldsymbol{x}^{(j)} \in \boldsymbol{\mathcal{X}}_{\mathrm{IS}}, j = 1, \ldots, N_{\mathrm{IS}}$. When the MPP is obtained from the FORM, a fair choice of $\Psi(\boldsymbol{X})$ is the standard normal distribution centered at that MPP [6]. Similar to the PDEM in Eq. (17), the $\hat{P}_f^{\mathrm{IS}}$ in Eq. (21) is also the sum of $P_f^{(j)}, j = 1, \ldots, N_{\mathrm{IS}}$. However, only those samples in the failure domain $\boldsymbol{\Omega}_F$ has non-zero value of $P_f^{(j)}$ in Eq. (21). Further, for each $\boldsymbol{x}^{(j)} \in \boldsymbol{\Omega}_F$, the $P_f^{(j)}$ has different value and depends on the location of the $\boldsymbol{x}^{(j)}$, but is unrelated to the specific value of the response $y_{\mathrm{EEV}}^{(j)}$. By contrast, Eqs. (17), (18) and (19) indicate that, although those representative points locating outside the ROI $\boldsymbol{\Omega}_{\mathrm{ROI}}$ have negligible values of $P_f^{(j)}$, they theoretically has non-zero value of $P_f^{(j)}$. Besides, for each $\boldsymbol{x}^{(j)} \in \boldsymbol{\Omega}_{\mathrm{ROI}}$, the magnitude of $P_f^{(j)}$ relies on the specific value of the response $y_{\mathrm{EEV}}^{(j)}$; see Fig. 1.

2.3 The existing AK-PDEM and its drawbacks

As stated in Section 2.2, the representative points in the ROI make critical contributions to the failure probability computed by the PDEM. Hence, the basic idea of the AK-PDEM is to iteratively refine the Kriging accuracy in the ROI, so as to ensure the accuracy of the estimated failure probability. Since the better Kriging accuracy is gained in the regions near the training samples, the AK-PDEM utilizes the learning function PIE to adaptively add the representative points within the ROI to their experimental designs until an appropriate convergence criterion is satisfied. For brevity, the Kriging theory is introduced in Appendix C, and the flowchart of the AK-PDEM is given as follows.

Algorithm 2:

(1) **Partition of probability space**. Generate the representative point set $\mathcal{X}_{\mathrm{RP}}=\left\{\boldsymbol{x}^{(1)},\ldots,\boldsymbol{x}^{(N_{\mathrm{RP}})}\right\}$ and compute the assigned probabilities $\mathcal{P}_{\mathrm{RP}}=\left\{p_{\mathrm{agn}}^{(1)},\ldots,p_{\mathrm{agn}}^{(N_{\mathrm{RP}})}\right\}$ via the GF discrepancy-based strategy. The $\mathcal{X}_{\mathrm{RP}}$ is taken as the candidate pool $\mathcal{X}_{\mathrm{CP}}$ in the subsequent process.

(2) **Initialization**. Generate the initial experimental design $\mathcal{X}=\left\{\boldsymbol{x}^{(1)},\ldots,\boldsymbol{x}^{(N_0)}\right\}$ via the Latin hypercube sampling (LHS) [32]; then, evaluate the computational model $\mathcal{M}$ on the $\mathcal{X}$ to gain $\mathcal{Y}=\left\{y_{\mathrm{EEV}}^{(j)}=\mathcal{M}\left(\boldsymbol{x}^{(j)}\right),j=1,\ldots,N_{\mathrm{RP}}\right\}$, together forming $\mathcal{D}=\left\{\mathcal{X},\mathcal{Y}\right\}$; N_0 is taken as $\max\left\{10,d+1\right\}$.

(3) **Calibration**. Calibrate the Kriging model $\hat{\mathcal{M}}^{\mathrm{K}}$ according to the current training dataset $\mathcal{D}$; see Appendix C.

(4) **Learning function**. A new training sample $\boldsymbol{x}_{\mathrm{new}}$ is selected from the current $\mathcal{X}_{\mathrm{CP}}$ via the PIE, that is,

$$\boldsymbol{x}_{\mathrm{new}}=\arg\max_{\boldsymbol{x}\in\mathcal{X}_{\mathrm{CP}}}\mathrm{PIE}\left(\boldsymbol{x}\right) \tag{22}$$

and the PIE is expressed as [21]

$$\begin{aligned}\mathrm{PIE}\left(\boldsymbol{x}\right)&=\left|-\int_{u_{\mathrm{thr}}-\varepsilon}^{+\infty}\ln\left(p_{\hat{Y}_{\mathrm{EEV}}}\left(\hat{y}\right)\right)p_{\hat{Y}_{\mathrm{EEV}}}\left(\hat{y}\right)d\hat{y}\right|\\&=\left|\begin{array}{l}\left(\ln\left(\sqrt{2\pi}\sigma_{\hat{y}}\left(\boldsymbol{x}\right)\right)+\dfrac{1}{2}\right)\cdot\left(1-\Phi\left(\dfrac{u_{\mathrm{thr}}-\varepsilon-\mu_{\hat{y}}\left(\boldsymbol{x}\right)}{\sigma_{\hat{y}}\left(\boldsymbol{x}\right)}\right)\right)\\+\dfrac{\left(u_{\mathrm{thr}}-\varepsilon-\mu_{\hat{y}}\left(\boldsymbol{x}\right)\right)}{2}\cdot\phi\left(\dfrac{u_{\mathrm{thr}}-\varepsilon-\mu_{\hat{y}}\left(\boldsymbol{x}\right)}{\sigma_{\hat{y}}\left(\boldsymbol{x}\right)}\right)\end{array}\right|\end{aligned} \tag{23}$$

in which $\mu_{\hat{y}}\left(\boldsymbol{x}\right)$ and $\sigma_{\hat{y}}\left(\boldsymbol{x}\right)$ are the mean and standard deviation of Kriging predictor $\hat{\mathcal{M}}^{\mathrm{K}}$; respectively. $\varepsilon=u_{\mathrm{thr}}-u_{\mathrm{ROI}}$ denotes the margin between the u_{thr} and the u_{ROI}. Since the true value of u_{ROI} is unavailable (Section 2.2) in the active-learning process, the margin ε is also unknown and is assumed to be proportional to the Kriging standard deviation, i.e., $\varepsilon\left(\boldsymbol{x}\right)\propto\sigma_{\hat{y}}\left(\boldsymbol{x}\right)$; $\Phi\left(\cdot\right)$ and $\phi\left(\cdot\right)$ are the cumulative distribution function (CDF) and the PDF of a standard normal variable, respectively.

(5) **Convergence criterion**. Check the following expression

$$\mathrm{PIE}_{\mathrm{new}}=\mathrm{PIE}\left(\boldsymbol{x}_{\mathrm{new}}\right)\le\varepsilon_{\mathrm{PIE}} \tag{24}$$

within 2 consecutive iterations, where $\varepsilon_{\mathrm{PIE}}$ is a specified tolerance. If Eq. (24) is satisfied, skip to Step (7), otherwise, continue with Step (6).

(6) **Update**. Evaluate the $\mathcal{M}$ on the $\boldsymbol{x}_{\text{new}}$, i.e., $y_{\text{new}}=\mathcal{M}\left(\boldsymbol{x}_{\text{new}}\right)$, then, $\mathcal{D}=\mathcal{D}\bigcup\left(\boldsymbol{x}_{\text{new}},y_{\text{new}}\right)$ and $\mathcal{X}_{\text{CP}}=\mathcal{X}_{\text{CP}}\setminus\boldsymbol{x}_{\text{new}}$.

(7) **Termination of active-learning process**. Evaluate the final Kriging model $\hat{\mathcal{M}}^{\text{K}}$ on the whole $\mathcal{X}_{\text{RP}}$, resulting in the predicted EEVs $\hat{\mathcal{Y}}_{\text{RP}}=\left\{\hat{y}_{\text{EEV}}^{(1)}=\hat{\mathcal{M}}^{\text{K}}\left(\boldsymbol{x}^{(1)}\right),\ldots,\hat{y}_{\text{EEV}}^{(N_{\text{RP}})}=\hat{\mathcal{M}}^{\text{K}}\left(\boldsymbol{x}^{(N_{\text{RP}})}\right)\right\}$.

(8) **GDEEs**. According to both the $\hat{\mathcal{Y}}_{\text{RP}}$ in Step (7) and the $\mathcal{P}_{\text{RP}}$ in Step (1), solve the associated N_{RP} GDEEs, resulting in $\left\{\hat{P}_f^{(1)},\ldots,\hat{P}_f^{(N_{\text{RP}})}\right\}$; see Eqs. (12) and (13).

(9) **Computation of failure probability**. The $\hat{P}_f$ is obtained based on $\left\{\hat{P}_f^{(1)},\ldots,\hat{P}_f^{(N_{\text{RP}})}\right\}$ via Eq. (17).

According to the parametric study in [21], it is desirable to specify $\varepsilon\left(\boldsymbol{x}\right)=1\cdot\sigma_{\hat{y}}\left(\boldsymbol{x}\right)$ and $\varepsilon_{\text{PIE}}=10^{-2}$, which enables the AK-PDEM (PIE) to provide a comparable estimate of failure probability to the standard PDEM.

In Algorithm 2, Step (1) shows that the sample size of representative points $\mathcal{X}_{\text{RP}}$ needs to be prescribed empirically in the existing AK-PDEM. This means that, although a Kriging with sufficient accuracy can be gained by the PIE, the inadequate size of $\mathcal{X}_{\text{RP}}$ may give rise to the resultant $\hat{P}_f$ deviating from the true one. Hence, a sequential PDEM that allows enriching sequentially the representative points is needed, serving as the outer loop of the existing AK-PDEM. This will be elucidated in Section 3.

3. The proposed AK-PDEMi

Section 3.1 outlines the sequential PDEM. Then, according to the sequential PDEM, a failure-informed enrichment algorithm is built in Section 3.2 to sequentially enrich the representative points in the outer loop. On this basis, the original AK-PDEM is improved by adding this outer loop. This is called the AK-PDEMi, and its numerical flowchart is presented in Section 3.3.

3.1 Sequential PDEM

As stated in Algorithm A1, the GF discrepancy-based strategy is employed to generate representative points in the standard PDEM, which involves both the iso-probabilistic transformation of Sobol sequence in the unit hypercube and the point set rearrangement, so as to minimize the GF-discrepancy of the point set (i.e., better uniformity). Clearly, the sequential PDEM still needs to follow this strategy.

The basic idea of the sequential PDEM is to enrich an initial representative point set $\mathcal{X}_{\text{RP}}$ of size N_{RP} with another new representative point set $\mathcal{X}_{\text{E},k}=\left\{\boldsymbol{x}^{(1)},\ldots,\boldsymbol{x}^{(N_{\text{E},k})}\right\}$ of size $N_{\text{E},k}$, that is, $\mathcal{X}_{\text{RP}}=\mathcal{X}_{\text{RP}}\bigcup\mathcal{X}_{\text{E},k}$ and $N_{\text{RP}}=N_{\text{RP}}+N_{\text{E},k}$, $k=1,2,\ldots$. During this process, the updated $\mathcal{X}_{\text{RP}}$ repartitions the whole probability space and the assigned probabilities $\mathcal{P}_{\text{RP}}$ are recomputed by Eq. (10). Then, the failure probability is recalculated by solving the increased number of GDEEs. This sequential process continues until a desired convergence criterion is fulfilled.

For illustration, Fig. 2 shows a toy example of a bivariate function $Y=\mathcal{M}\left(X_1,X_2\right)=X_1^2+X_2^2$, where both X_1 and X_2 are standard uniform variables. The failure probability is defined as $P_f=\Pr\left\{y\gg u_{\text{thr}}\right\}$, with the u_{thr} being taken as 1.71, and the crude MCS is performed as reference. First, an initial representative point set

$\mathcal{X}_{\mathrm{RP}}=\left\{\boldsymbol{x}^{(1)},\ldots,\boldsymbol{x}^{(40)}\right\}$ of size 40 is shown in Fig. 2(a), where the Voronoi cells of these representative points are plotted to graphically represent their assigned probabilities. Note that the assigned probability of a point is equal to the area of its Voronoi cell in the case of uniform distribution; see Eqs. (10) and (11). Due to the sparsity of $\mathcal{X}_{\mathrm{RP}}$, only 1 representative point is located in the ROI, and the assigned probability, $p_{\mathrm{assign}}^{(j)}$, of each representative point has significant value; see Fig. 2(b). According to Eq. (16), the area enclosed by $p_{Y_{\mathrm{EEV}}}^{(j)}(y)$ and the horizontal axis is exactly equal to the $p_{\mathrm{assign}}^{(j)}$. Hence, the main body of $p_{Y_{\mathrm{EEV}}}^{(j)}(y)$ is very steep, and the resultant $p_{Y_{\mathrm{EEV}}}(y)$ deviates from the histogram of the MCS, as shown in Fig. 2(c). Clearly, the insufficient size of $\mathcal{X}_{\mathrm{RP}}$ gives rise to a poor performance of the PDEM.

To enhance the performance of the PDEM, the existing $\mathcal{X}_{\mathrm{RP}}$ is enriched with another new representative point set $\mathcal{X}_{\mathrm{E}}=\left\{\boldsymbol{x}^{(1)},\ldots,\boldsymbol{x}^{(1200)}\right\}$, that is, $\mathcal{X}_{\mathrm{RP}}=\mathcal{X}_{\mathrm{RP}}\bigcup\mathcal{X}_{\mathrm{E}}$. As shown in Fig. 2(d), the updated $\mathcal{X}_{\mathrm{RP}}$ repartitions the whole probability space and the values of assigned probabilities are reduced significantly; see Fig. 2(e). Then, the partial PDF $p_{Y_{\mathrm{EEV}}}^{(j)}(y)$ becomes flat and the resultant $p_{Y_{\mathrm{EEV}}}(y)$ is consistent with the histogram of the MCS, as shown in Fig. 2(f). Clearly, as the sample size of $\mathcal{X}_{\mathrm{RP}}$ increases, the performance of PDEM is improved accordingly.

Fig. 2(d) shows that the enriched representative points $\mathcal{X}_{\mathrm{E}}$ are scattered in the whole probability space. Among the $\mathcal{X}_{\mathrm{E}}$, only a small amount of representative points in the ROI, denoted by $\mathcal{X}_{\mathrm{E}}^{\mathrm{ROI}}=\left\{\boldsymbol{x}^{(1)},\ldots,\boldsymbol{x}^{\left(N_{\mathrm{E}}^{\mathrm{ROI}}\right)}\right\}$ of size $N_{\mathrm{E}}^{\mathrm{ROI}}$, make critical contributions to the P_f^{PDEM} (Section 2.2). In view of this, it seems more efficient to enrich the existing $\mathcal{X}_{\mathrm{RP}}$ with only the representative points $\mathcal{X}_{\mathrm{E}}^{\mathrm{ROI}}$ in the ROI, that is, $\mathcal{X}_{\mathrm{RP}}=\mathcal{X}_{\mathrm{RP}}\bigcup\mathcal{X}_{\mathrm{E}}^{\mathrm{ROI}}$, and $N_{\mathrm{RP}}=N_{\mathrm{RP}}+N_{\mathrm{E}}^{\mathrm{ROI}}$. This enrichment treatment is called Scenario-1, and the sample distribution of the updated $\mathcal{X}_{\mathrm{RP}}$ in Scenario-1 is shown in Fig. 2(g). In comparison with Fig. 2(d), the Voronoi cells of representative points near the boundary of the ROI are much greater. This difference is attributed to that the boundary of ROI lies in the interface between the sparse $\mathcal{X}_{\mathrm{RP}}$ and the dense $\mathcal{X}_{\mathrm{E}}^{\mathrm{ROI}}$, and the Voronoi cells of the representative points in this interface take up some extra areas out of the ROI. As a result, their assigned probabilities are greater than those in other regions; see Fig. 2(h), and the main bodies of their partial PDFs are far greater than others, giving rise to the slight overestimate of $p_{Y_{\mathrm{EEV}}}(y)$ near the vertical axis of $y=u_{\mathrm{thr}}$, as enclosed by red dashed ellipse in Fig. 2(i).

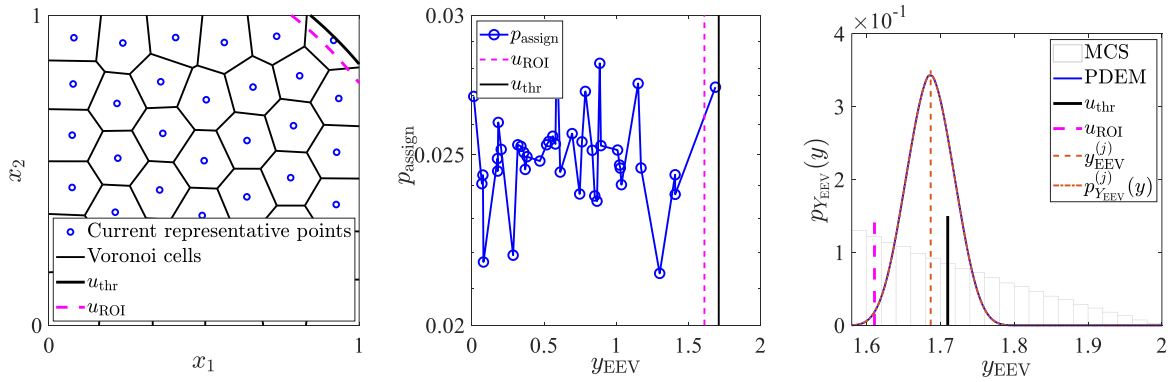

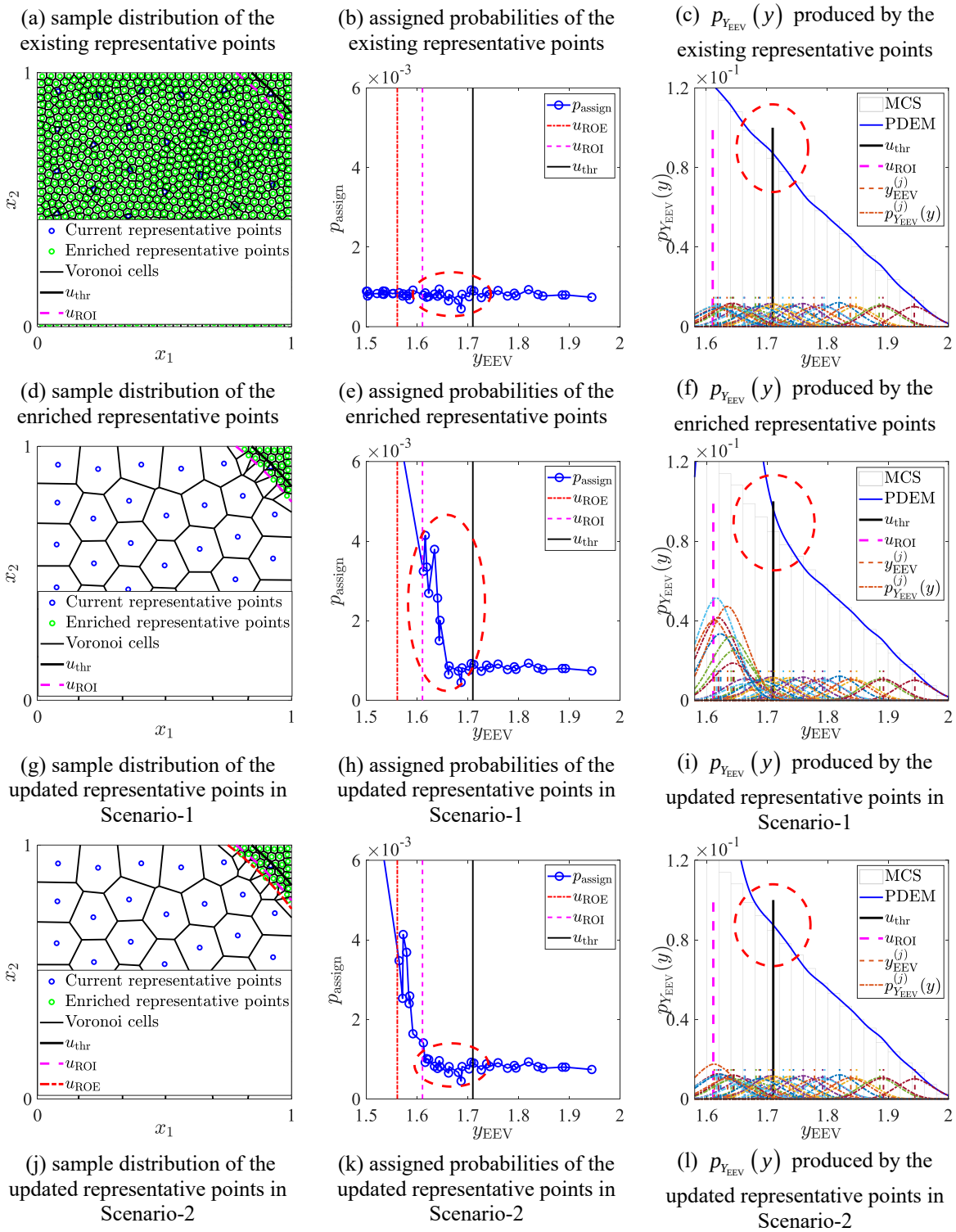

Fig.2 Comparison of different enrichment scenarios

To avoid this, the sub-region covered by the enriched representative points need to be extended to some degree, and this is called the region of enrichment (ROE) such that

$$\boldsymbol{\Omega}_{\mathrm{ROE}} = \left\{ \boldsymbol{x} \middle| y_{\mathrm{EEV}} = \mathcal{M}(\boldsymbol{x}) \geq u_{\mathrm{ROE}} \right\} \tag{25}$$

where u_{ROE} is the boundary of the ROE. Obviously, the range of the $\boldsymbol{\Omega}_{\mathrm{ROE}}$ varies with the problems under consideration. Hence, the interval $u_{\mathrm{ROI}} - u_{\mathrm{ROE}}$ is assumed to be proportional to the interval $u_{\mathrm{thr}} - u_{\mathrm{ROI}}$ herein.

Based on the authors' experience, it is feasible to specify $\left(u_{\mathrm{ROI}}-u_{\mathrm{ROE}}\right)/\left(u_{\mathrm{thr}}-u_{\mathrm{ROI}}\right)=0.5$, yielding

$$u_{\mathrm{ROE}}=1.5\cdot u_{\mathrm{ROI}}-0.5\cdot u_{\mathrm{thr}} \tag{26}$$

Among the $\mathcal{X}_{\mathrm{E}}$, the enriched representative points in the ROE are denoted by $\mathcal{X}_{\mathrm{E}}^{\mathrm{ROE}}=\left\{\boldsymbol{x}^{(1)},\ldots,\boldsymbol{x}^{\left(N_{\mathrm{E}}^{\mathrm{ROE}}\right)}\right\}$ of size $N_{\mathrm{E}}^{\mathrm{ROE}}$; then, the initial representative point set $\mathcal{X}_{\mathrm{RP}}$ is enriched with the $\mathcal{X}_{\mathrm{E}}^{\mathrm{ROE}}$, i.e., $\mathcal{X}_{\mathrm{RP}}=\mathcal{X}_{\mathrm{RP}}\bigcup\mathcal{X}_{\mathrm{E}}^{\mathrm{ROE}}$, and $N_{\mathrm{RP}}=N_{\mathrm{RP}}+N_{\mathrm{E}}^{\mathrm{ROE}}$. This enrichment treatment is called Scenario-2, and the sample distribution of the updated $\mathcal{X}_{\mathrm{RP}}$ in Scenario-2 is shown in Fig. 2(j). Thanks to these extra representative points located between the u_{ROE} and the u_{ROI}, the Voronoi cells of representative points in the ROI have approximate sizes. As a result, similar values of the assigned probabilities in the ROI are shown in Fig. 2(k). Then, the main body of $p_{Y_{\mathrm{EEV}}}^{(j)}\left(y\right)$ in the ROI is similar to each other, and the $p_{Y_{\mathrm{EEV}}}\left(y\right)$ agrees well with the histogram of MCS near the vertical axis of $y=u_{\mathrm{thr}}$, see Fig. 2(l). Thanks to the enrichment of representative points in the ROE, Scenario-2 makes fine partitions of the ROI and yields consistent failure probability to the treatment of enrichment in the whole probability space. Hence, Scenario-2 is chosen in the sequential PDEM.

As shown in Figs. 2 (j-l), the implementation of Scenario-2 is based on the true value of u_{ROI} (further u_{ROE}); whereas, the true value of u_{ROI} is a byproduct of the standard PDEM and totally unknown *a priori*. Moreover, the process of selecting the $\mathcal{X}_{\mathrm{E}}^{\mathrm{ROE}}$ from the $\mathcal{X}_{\mathrm{E}}$ via Eq. (25) entails N_{E} runs of computational model evaluations. This implies that, in comparison with the enrichment in the whole probability space (Figs. 2(d-f)), Scenario-2 actually does not reduce the number of computational model evaluations at all. These two issues will be addressed when the enrichment scheme of Scenario-2 is implemented in the outer loop of the AK-PDEM, and are stated in the next section.

Remark 4: The separate utilities of the ROE and the ROI are elucidated as follows. The ROI defines the sub-region where the representative points make critical contributions to the failure probability (Section 2.2), thereby the inner loop tries to adaptively refine the Kriging accuracy in the ROI via the learning function PIE, so as to alleviate the Kriging-induced error in the estimated failure probability. By contrast, Eqs. (25) and (26) show that the range of the ROE is slightly greater than that of the ROI, and the extra margin between the u_{ROE} and the u_{ROI} aims to guarantee that, in the range of the ROI, both the magnitude of the assigned probabilities and the partial PDF curves of the representative points in Figs. 2(j-l) are consistent with those of the representative points enriched in the whole probability space (Figs. 2(d-f)). In essence, the notation of the ROE aims to ensure that the representative points located in the ROI still follows the GF discrepancy-based criterion, so as to reduce the PDEM-associated discretization error.

3.2 Failure-informed enrichment algorithm

When the enrichment scheme of Scenario-2 is implemented in the outer loop of the AK-PDEM, the sequential enrichment in the ROE and the adaptive refinement of Kriging model are complementary. Specifically, when a Kriging model $\hat{\mathcal{M}}^{\mathrm{K}}$ is trained at the end of the existing AK-PDEM, both the $\hat{\mathcal{Y}}_{\mathrm{RP}}$ and the $\left\{\hat{P}_f^{(1)},\ldots,\hat{P}_f^{(N_{\mathrm{RP}})}\right\}$ can be obtained from Steps (7) and (8) in Algorithm 2, respectively. Then, substitute them into Algorithm B1, an estimate

of the u_{ROI}, i.e., $\hat{u}_{\mathrm{ROI}}$, can be obtained readily. Moreover, since the $\hat{\mathcal{M}}^{\mathrm{K}}$ serves as a cheap proxy of the actual computational model $\mathcal{M}$, the process of selecting the representative points in the ROE $\boldsymbol{\mathcal{X}}_{\mathrm{E}}^{\mathrm{ROE}}$ from the $\boldsymbol{\mathcal{X}}_{\mathrm{E}}$ can be conducted based on the Kriging $\hat{\mathcal{M}}^{\mathrm{K}}$, and this treatment incurs no extra computational model evaluations.

However, these two treatments may incur the following potential risk. If the Kriging $\hat{\mathcal{M}}^{\mathrm{K}}$ is not sufficiently accurate, the value of $\hat{u}_{\mathrm{ROI}}$ (further $\hat{u}_{\mathrm{ROE}}$) may not be accurate enough. In this case, the resultant $\boldsymbol{\mathcal{X}}_{\mathrm{E}}^{\mathrm{ROE}}$ may be not totally located in the ROE. Whereas, after several runs of the outer-loop enrichment in the ROE and the inner-loop adaptive refinement of Kriging model, the Kriging accuracy in the ROI is expected to be improved, and the $\hat{u}_{\mathrm{ROI}}$, as well as the $\hat{u}_{\mathrm{ROE}}$, gradually coincides with the true one. In this regard, the Kriging-assisted enrichment process becomes gradually consistent with Scenario-2. For clarity, the representative points $\boldsymbol{\mathcal{X}}_{\mathrm{E}}^{\mathrm{ROE}}$ in the ROE are reformulated as the $\tilde{\boldsymbol{\mathcal{X}}}_{\mathrm{RP}}$ hereinafter. Based on the authors' experience, the sample size of initial representative point set $\boldsymbol{\mathcal{X}}_{\mathrm{RP}}$ is taken as 2000, and the number of the enriched representative points $\tilde{\boldsymbol{\mathcal{X}}}_{\mathrm{RP}}$ in each loop is taken as 10.

As stated in Section 1, the PDEM is not equipped with the COV-like matric; hence, the outer-loop convergence criterion is defined based on the stabilization of the estimated failure probabilities, that is,

$$\left|\hat{P}_f^{(j)} - \hat{P}_f^{(j-1)}\right| \Big/ \hat{P}_f^{(j-1)} \le \varepsilon_{\hat{P}_f} \tag{27}$$

within 2 successive loops, where $\hat{P}_f^{(j)}$ and $\hat{P}_f^{(j-1)}$ denote the failure probability computed at the j-th and (j-1)-th outer loop, respectively; the tolerance $\varepsilon_{\hat{P}_f}$ is taken as 0.5% here.

Since this enrichment process entails the valuable failure-associated information provided by the Kriging model in the previous inner loop, this is called the failure-informed enrichment scheme. As stated in Section 3.1, the generation of the enriched representative points by the failure-informed enrichment scheme still needs to follow the GF discrepancy-based criterion (Appendix A). Hence, both the iso-probabilistic transformation of Sobol sequence in the unit hypercube (Eq. (A4)) and the point set rearrangement (Eq. (A5)) are naturally involved in the failure-informed enrichment scheme accordingly. The corresponding flowchart is provided in Algorithm 3.

Algorithm 3: Generation of new representative points in the failure-informed enrichment scheme

Input: The $\hat{u}_{\mathrm{ROE}}$, the Kriging $\hat{\mathcal{M}}^{\mathrm{K}}$ and the $\boldsymbol{\mathcal{X}}_{\mathrm{RP}}$ in the previous inner loop.
Initialization:
  The target sample size $N_{\mathrm{target}} = 10$, the initial $N_0 = 100$, and the increment $N_{\mathrm{inc}} = 100$.
Iterative algorithm: In step k = 1, 2, …,
  Generate the point set $\boldsymbol{\mathcal{U}}_0 = \left\{\boldsymbol{u}^{(1)}, \ldots, \boldsymbol{u}^{(N_0)}\right\}$ from the Sobol sequence in the unit hypercube.
  Convert the $\boldsymbol{\mathcal{U}}_0$ to the $\boldsymbol{\mathcal{X}}_0 = \left\{\boldsymbol{x}^{(1)}, \ldots, \boldsymbol{x}^{(N_0)}\right\}$ via the isoprobabilistic transformation in Eq. (A4).
  Evaluate the $\hat{\mathcal{M}}^{\mathrm{K}}$ on the $\boldsymbol{\mathcal{X}}_0$, yielding $\hat{\boldsymbol{\mathcal{Y}}}_0 = \left\{\hat{y}_{\mathrm{EEV}}^{(1)}, \ldots, \hat{y}_{\mathrm{EEV}}^{(N_0)}\right\}$.
  According to the $\hat{\boldsymbol{\mathcal{Y}}}_0$, select the points in the ROE, i.e., the $\boldsymbol{\mathcal{X}}_1$ of size N_1, from the $\boldsymbol{\mathcal{X}}_0$.
  If $N_1 \ge N_{\mathrm{target}}$, then
    Break.
  else
    $N_0 = N_0 + N_{\mathrm{inc}}$, and $k = k + 1$
  End
According to Eq. (A5), conduct the rearrangement of $\boldsymbol{\mathcal{X}}_1$, yielding the rearranged point set $\boldsymbol{\mathcal{X}}_2$.

15: **Return:** The final enriched representative point set $\tilde{\mathcal{X}}_{\mathrm{RP}} = \mathcal{X}_2$.

Remark 5: In the failure-informed enrichment scheme, the Kriging $\hat{\mathcal{M}}^{\mathrm{K}}$ is employed to provide the $\hat{u}_{\mathrm{ROI}}$ based on Algorithm B1, and the trial-and-error approach in Algorithm B1 ensures that the value of the $\hat{u}_{\mathrm{ROI}}$ is equal to or less than the threshold u_{thr}. If an ill-calibrated Kriging is produced in the initial stage, the ROI $\boldsymbol{\Omega}_{\mathrm{ROI}} = \{\boldsymbol{x} | \hat{y}_{\mathrm{EEV}} \geq u_{\mathrm{ROI}}\}$ and, further, the ROE $\boldsymbol{\Omega}_{\mathrm{ROE}} = = \{\boldsymbol{x} | \hat{y}_{\mathrm{EEV}} \geq u_{\mathrm{ROE}}\}$ estimated by this poor Kriging are different from the true ones. Whereas, the outer-loop stopping condition in Eq. (27) ensures that at least 3 loops will be performed in the initial stage of the AK-PDEMi. Hence, despite a poor Kriging may be initially calibrated, the outer and inner loops continue and the Kriging accuracy in the range of the ROE will be gradually improved by continuously adding new training samples to the experimental designs. Obviously, these two treatments, i.e., fulfilling Eq. (27) within 2 consecutive loops and specifying a relatively minor tolerance $\varepsilon_{\hat{P}_f}$, attempt to avoid the undesired premature termination.

Remark 6: The inner-loop convergence criterion in Eq. (24) aims to minimize the Kriging-induced error as much as possible, while the outer-loop convergence criterion in Eq. (27) pursues reducing the PDEM-associated discretization error. With respect to the inner-loop convergence criteria, three basic types are available in the existing literature, i.e., the ones based on learning function values, the ones based on the confidence bound of the estimated failure probability, and the ones based on the stabilization of failure probability estimates, as stated in Section 1. The stopping condition in Eq. (24) is defined based on the learning function PIE values and was shown to provide a desired performance in previous study [21]. With respect to the outer-loop convergence criteria, the convergence of simulation methods is generally assessed according to the COV of failure probability, e.g., $\mathrm{COV}_{\hat{P}_f} \leq 5\%$; on the contrary, the PDEM is not equipped with the COV-like metric. In view of this, the convergence criterion (Eq. (27)) associated with the stabilization of failure probability estimates is employed here. Note that this convergence criterion reflects the variation of failure probabilities within 2 consecutive loops, rather than 2 iterative steps of the inner loop. Hence, this aims to measure the influence of the sequential generation of new representative points by the outer loop on the failure probability, and it is necessary to distinguish this outer-loop convergence criterion from those inner-loop stopping condition associated with the stabilization of failure probability estimates in the existing literature. Clearly, Eqs. (24) and (27) together attempt to ensure the convergence of the AK-PDEMi.

3.3 Numerical procedure of the proposed AK-PDEMi

When the failure-informed enrichment scheme in Section 3.2 is added into the existing AK-PDEM in Section 2.3, serving as the outer loop, the outer and inner loops are complementary and proceed sequentially until both of their convergence criteria are satisfied. This is called the AK-PDEMi. The corresponding flowchart is presented in Fig. 3, with the main steps given as follows.

Algorithm 4:

(1) **The partition of probability space.** Generate the representative point set $\mathcal{X}_{\mathrm{RP}}$ and compute its assigned probabilities $\mathcal{P}_{\mathrm{RP}}$ using the GF discrepancy-based strategy; see Appendix A. The $\mathcal{X}_{\mathrm{RP}}$ is taken as the candidate pool $\mathcal{X}_{\mathrm{CP}}$.

(2) **Initialization.** Generate the initial experimental design $\mathcal{X}=\left\{\boldsymbol{x}^{(1)},\ldots,\boldsymbol{x}^{(N_0)}\right\}$ and obtain the corresponding computational model evaluations $\mathcal{Y}=\left\{y_{\mathrm{EEV}}^{(1)},\ldots,y_{\mathrm{EEV}}^{(N_0)}\right\}$, resulting in $\mathcal{D}=\{\mathcal{X},\mathcal{Y}\}$.

(3) **Calibration.** Train the Kriging model $\hat{\mathcal{M}}^{\mathrm{K}}$ based on the current $\mathcal{D}$; see Appendix C.

(4) **Learning function**. Select the $\boldsymbol{x}_{\mathrm{new}}$ from the current $\mathcal{X}_{\mathrm{CP}}$ via the PIE; see Eq. (22).

(5) **The inner-loop convergence criterion**. If the PIE-related stopping condition in Eq. (24) is not satisfied, go to Step (6), otherwise, skip to Step (7).

(6) **Update**. Evaluate the computational model $\mathcal{M}$ on the $\boldsymbol{x}_{\mathrm{new}}$, i.e., $y_{\mathrm{new}}=\mathcal{M}\left(\boldsymbol{x}_{\mathrm{new}}\right)$; then, $\mathcal{D}=\mathcal{D}\bigcup\left(\boldsymbol{x}_{\mathrm{new}},y_{\mathrm{new}}\right)$ and $\mathcal{X}_{\mathrm{CP}}=\mathcal{X}_{\mathrm{CP}}\setminus\boldsymbol{x}_{\mathrm{new}}$.

(7) **Termination of the inner loop**. Evaluate the final Kriging model $\hat{\mathcal{M}}^{\mathrm{K}}$ on the current $\mathcal{X}_{\mathrm{RP}}$, resulting in the predicted EEVs $\hat{\mathcal{Y}}_{\mathrm{RP}}=\left\{\hat{y}_{\mathrm{EEV}}^{(j)}=\hat{\mathcal{M}}\left(\boldsymbol{x}^{(N_{\mathrm{RP}})}\right),j=1,\ldots,N_{\mathrm{RP}}\right\}$.

(8) **GDEEs**. According to both the predicted EEVs $\hat{\mathcal{Y}}_{\mathrm{RP}}$ in Step (7) and the assigned probabilities $\mathcal{P}_{\mathrm{RP}}$, solve the associated N_{RP} GDEEs, resulting in $\left\{\hat{P}_f^{(1)},\ldots,\hat{P}_f^{(N_{\mathrm{RP}})}\right\}$; see Eqs. (12) and (13).

(9) **Computation of failure probability**. The P_f is computed based on $\left\{\hat{P}_f^{(1)},\ldots,\hat{P}_f^{(N_{\mathrm{RP}})}\right\}$ via Eq. (17).

(10) **The outer-loop convergence criterion**. If Eq. (27) is not satisfied, continue to Step (11), otherwise, skip to Step (14).

(11) **Determination of both the $\hat{u}_{\mathrm{ROI}}$ and the $\hat{u}_{\mathrm{ROE}}$**. Substitute both the $\hat{\mathcal{Y}}_{\mathrm{RP}}$ in Step (7) and the $\left\{\hat{P}_f^{(1)},\ldots,\hat{P}_f^{(N_{\mathrm{RP}})}\right\}$ in Step (8) into Algorithm B1, resulting in the $\hat{u}_{\mathrm{ROI}}$; then, the $\hat{u}_{\mathrm{ROE}}$ is calculated via Eq. (26).

(12) **Failure-informed enrichment process**. Generate another new set of representative points $\tilde{\mathcal{X}}_{\mathrm{RP}}=\left\{\boldsymbol{x}^{(1)},\ldots,\boldsymbol{x}^{(\tilde{N}_{\mathrm{RP}})}\right\}$ via Algorithm 3.

(13) **The repartition of probability space**. Enrich both the $\mathcal{X}_{\mathrm{RP}}$ and the $\mathcal{X}_{\mathrm{CP}}$ with the $\tilde{\mathcal{X}}_{\mathrm{RP}}$, that is, $\mathcal{X}_{\mathrm{RP}}=\mathcal{X}_{\mathrm{RP}}\bigcup\tilde{\mathcal{X}}_{\mathrm{RP}}$, $\mathcal{X}_{\mathrm{CP}}=\mathcal{X}_{\mathrm{CP}}\bigcup\tilde{\mathcal{X}}_{\mathrm{RP}}$, and $N_{\mathrm{RP}}=N_{\mathrm{RP}}+\tilde{N}_{\mathrm{RP}}$. Then, the assigned probabilities $\mathcal{P}_{\mathrm{RP}}$ of the updated $\mathcal{X}_{\mathrm{RP}}$ are recomputed via Eq. (10); finally, return to Step (3).

(14) **Termination of the outer loop**. The $\hat{P}_f$ at the current loop is taken as the final result of the AK-PDEMi.

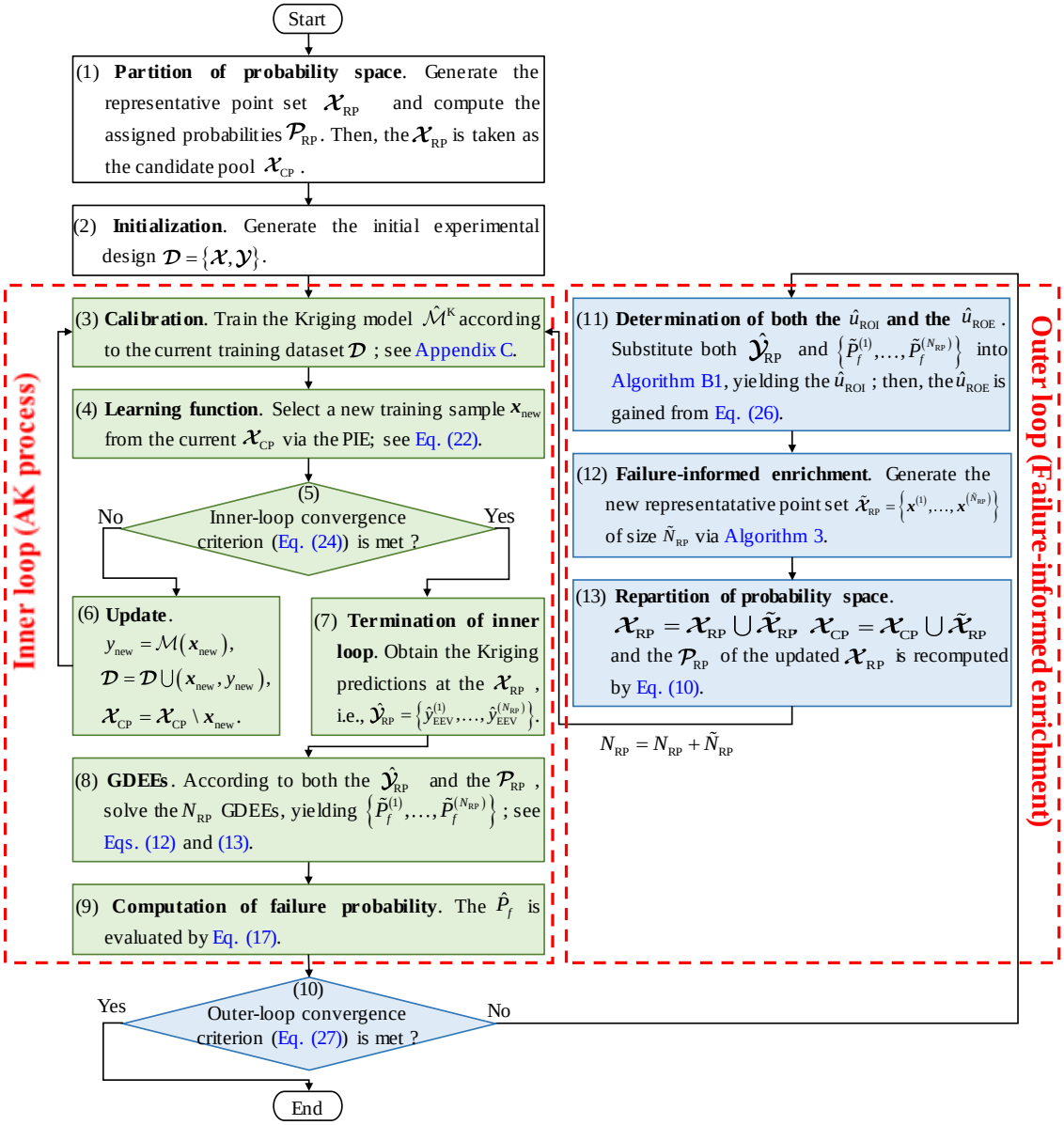

Fig. 3 Flowchart of the proposed AK-PDEMi

Remark 7: In comparison with the existing AK-PDEM that only partitions the probability space at the first step (green blocks in Fig. 3), the AK-PDEMi enables to sequentially repartition the probability space based on the additional representative points generated by the failure-informed enrichment scheme in each outer loop (blue blocks in Fig. 3). Since most of the enriched representative points are expected to be located in the ROE, fine partitions are made in the range of the ROI, thereby the PDEM-associated discretization error is expected to be reduced accordingly. Hence, the AK-PDEMi not only reduces the Kriging-induced error, but also alleviates the PDEM-associated discretization error.

4. Illustrating examples

Three numerical examples are studied to show the efficacy of the proposed AK-PDEMi. The crude MCS is performed to provide the reference value $\hat{P}_f^{MCS}$. Comprehensive comparisons are made between the proposed AK-PDEMi and other existing reliability analysis algorithms, including the FORM, the IS, the SuS, the AK-MCS, the APCK-IS, the APCK-SuS, the standard PDEM and the existing AK-PDEM.

In the IS, the MPP is obtained from the result of the FORM, then, the importance distribution takes the standard normal distribution centered at the MPP [6]. In the SuS, the conditional probability is 0.1 and the sample size of each subset is taken as 2000. In the AK-MCS, the U learning function is employed, and the stopping condition is defined such that $\min_{\boldsymbol{x}} U(\boldsymbol{x}) \geq 2$. In both the APCK-IS and the APCK-SuS, the Polynomial Chaos-Kriging (PCK) model [25] and the U learning function are adopted; the stopping condition is defined in terms of the bound of the estimated failure probability in 2 successive iterations, with the tolerance being 1×10^{-2} [13]; the sample size of each subset in the SuS is taken as 10^5. For more details, the reader is referred to [13]. In the standard PDEM, the sample size of representative points is taken as 2000, exactly equal to the initial representative point size of the AK-PDEMi; the AK-PDEM corresponds exactly to the first run of the AK process in the AK-PDEMi, which is denoted as the 0-th loop hereafter. Moreover, the maximum number of computational model evaluations for these active learning-based algorithms is set as 500.

The simulation methods and active learning-based methods are replicated 10 times to consider their statistical uncertainties; then, the median, the 25-th and the 75-th quantiles, denoted as q_{25} and q_{75}, of the 10 replications are provided. The accuracy of different reliability analysis algorithms is measured by the relative error against the P_f^{MCS}, that is, $\delta_{\hat{P}_f} = \left|\hat{P}_f - \hat{P}_f^{\mathrm{MCS}}\right| \Big/ \hat{P}_f^{\mathrm{MCS}} \times 100\%$; the efficiency of various reliability methods is quantified by the total number, N_{call}, of calls to computational model.

4.1 A series system with four branches

The P_f for a series system with four branches is defined as [14]

$$P_f = \Pr\left\{\begin{array}{l} \left(-0.1\left(X_1 - X_2\right)^2 + \left(X_1 + X_2\right)/\sqrt{2} \geq a\right) \\ \cup\left(-0.1\left(X_1 - X_2\right)^2 - \left(X_1 + X_2\right)/\sqrt{2} \geq a\right) \\ \cup\left(X_2 - X_1 \geq b/\sqrt{2}\right) \\ \cup\left(X_1 - X_2 \geq b/\sqrt{2}\right) \end{array}\right\} \tag{28}$$

where X_1 and X_2 are standard normal variables, respectively; the constants a and b are taken as 3.5 and 7.5, respectively. Then, Eq. (28) is equivalent to $P_f = \Pr\left\{Y_{\mathrm{EEV}} \geq \dfrac{b}{\sqrt{2}}\right\} = \int_{\frac{b}{\sqrt{2}}}^{+\infty} p_{Y_{\mathrm{EEV}}}(y)dy$, with the Y_{EEV} expressed as

$$Y_{\mathrm{EEV}} = \max\left\{\begin{array}{l} -0.1\left(X_1 - X_2\right)^2 + \left(X_1 + X_2\right)/\sqrt{2} + b/\sqrt{2} - a \\ -0.1\left(X_1 - X_2\right)^2 - \left(X_1 + X_2\right)/\sqrt{2} + b/\sqrt{2} - a \\ X_2 - X_1 \\ X_1 - X_2 \end{array}\right\} \tag{29}$$

Fig. 4 shows the performance of the proposed AK-PDEMi for Example 1, and a total of $N_{\mathrm{loop}} = 7$ outer and inner loops are involved. In Fig. 4(a), the enriched representative points generated in each outer loop are plotted as the colored markers, which are generally located in the range of the ROE. As a result, the Voronoi cells of these representative points in the ROI are reduced rapidly, and their assigned probabilities in the ROI are far smaller than those in other regions; see Fig. 4(b). Then, Fig. 4(c) shows the convergence performance of the inner loops of the AK-PDEMi. As given in Eq. (24), the inner loop is converged when $\mathrm{PIE}_{\mathrm{new}} \leq \varepsilon_{\mathrm{PIE}}$ in 2 successive iterations,

and there are 7 descending branches in the PIE curves. In each outer loop, at least 10 new representative points are generated by the failure-informed enrichment scheme (Algorithm 3); whereas, only a fraction of these new representative points will be selected as training samples in the inner loop. This is attributed to that these outer-loop-generated representative points are scattered in the ROE, but the inner loop aims to only select training samples in the ROI, so as to secure the Kriging accuracy in the ROI; see Fig. 4(d). As a result, the Kriging predictions $\hat{\mathcal{Y}}_{\mathrm{RP}}$ coincide well with the true counterparts $\mathcal{Y}_{\mathrm{RP}}$ in the ROI; see Fig. 4(e). The $p_{Y_{\mathrm{EEV}}}(y)$ curves in the all loops of the AK-PDEMi are shown in Fig. 4(f). As stated above, the AK-PDEM corresponds to the 0-st loop of the AK-PDEMi. The $p_{Y_{\mathrm{EEV}}}(y)$ produced by the AK-PDEM accords with that produced by the standard PDEM, but deviates from the histogram of the crude MCS, owing to the insufficiency of the initial 2000 representative points. On the contrary, as the outer and inner loops of the AK-PDEMi proceed sequentially, the resultant $p_{Y_{\mathrm{EEV}}}(y)$ finally coincides with the histogram of the MCS. The evolution of both $\hat{u}_{\mathrm{ROI}}$ and $\hat{P}_f$ against N_{loop} are shown in Figs. 4(g) and 4(h), respectively, and the $\hat{P}_f$ converges gradually to the reference value $\hat{P}_f^{\mathrm{MCS}}$.

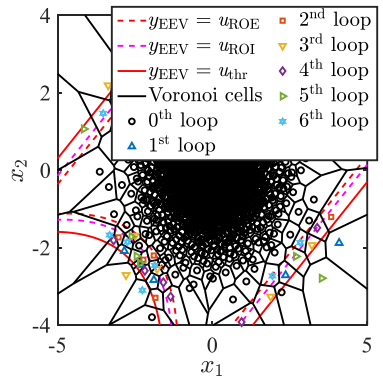

(a) sample distribution of the enriched representative points

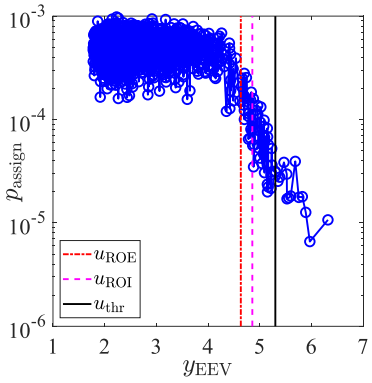

(b) $\mathcal{P}_{\mathrm{RP}}$

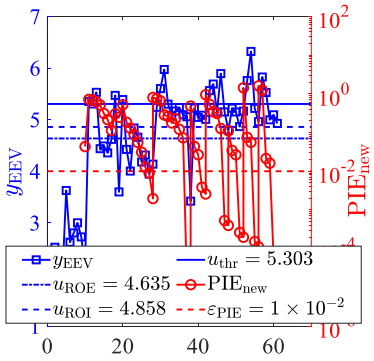

(c) evolution of both y_{new} and $\mathrm{PIE}_{\mathrm{new}}$ against N_{call}

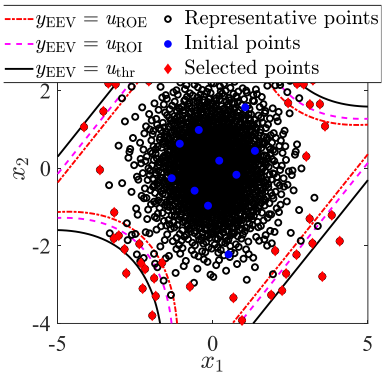

(d) sample distribution of training samples

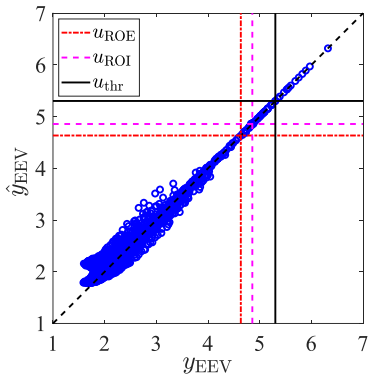

(e) $\mathcal{Y}_{\mathrm{RP}}$ vs. $\hat{\mathcal{Y}}_{\mathrm{RP}}$

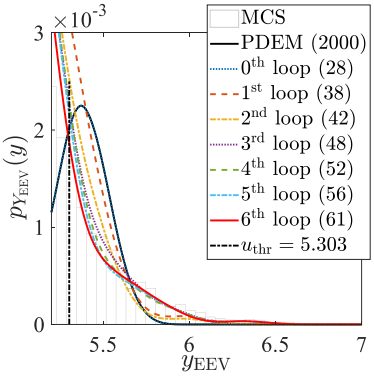

(f) $p_{Y_{\mathrm{EEV}}}(y)$

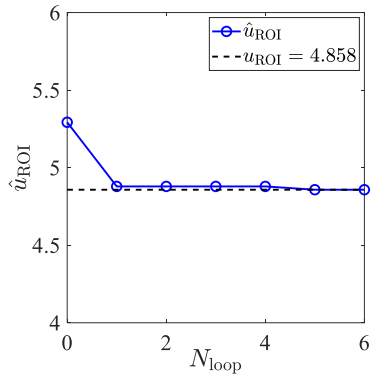

(g) evolution of $\hat{u}_{\mathrm{ROI}}$ against N_{loop}

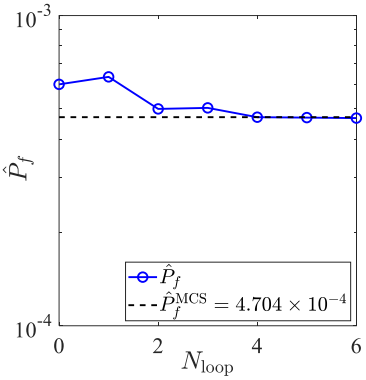

(h) evolution of $\hat{P}_f$ against N_{loop}

Fig. 4 Performance of the AK-PDEMi for Example 1

Table 1 lists the results of different reliability analysis algorithms for Example 1. Both the FORM and the IS fail to produce fair estimates of failure probability, due to the existence of multiple MPPs. The median of the failure probability estimates provided by the SuS also deviates from the reference value $\hat{P}_f^{\mathrm{MCS}}$. Similar to the IS, all the 10 replicates of the APCK-IS only identify one limit state, giving rise to a poor estimate of failure probability. Among the 10 repeated runs of the AK-MCS and the APCK-SuS, the number of limit states identified by them varies from 1 to 4, and the median of the failure probability estimates deviates from the $\hat{P}_f^{\mathrm{MCS}}$. The AK-PDEM provides a comparable estimate of failure probability to the standard PDEM, but diverges from the $\hat{P}_f^{\mathrm{MCS}}$. By comparison, the $\hat{P}_f$ offered by the AK-PDEMi becomes consistent with the crude MCS with fair efficiency.

Table 1. Comparisons of different reliability algorithms in Example 1

Method	N_{call}		$\hat{P}_f$ $(\times 10^{-4})$		$\delta_{\hat{P}_f}$ (%)
	Median	$[q_{25}, q_{75}]$	Median	$[q_{25}, q_{75}]$	
MCS	5×10^7	-	4.704	-	-
FORM	12	-	2.326	-	50.54
IS	4012	[4012, 4012]	1.454	[1.403, 1.490]	69.09
SuS	6919	[6913, 6930]	3.208	[2.820, 4.820]	31.81
AK-MCS	44.5	[43, 57]	3.040	[2.685, 4.175]	35.37
APCK-IS	50.5	[41, 57]	0.896	[0.872, 1.428]	80.95
APCK-SuS	153.5	[62, 226]	3.056	[2.106, 3.773]	35.03
PDEM	2000	-	6.001	-	27.58
AK-PDEM	29	[28, 29.5]	6.001	[6.001, 6.001]	27.58
AK-PDEMi	60.5	[59, 64.5]	4.565	[4.489, 4.598]	2.95

4.2 A 20-dimensional nonlinear function

The second example considers a 20-dimensional nonlinear function such that [33]

$$Y = \frac{1}{20}\left(X_1^2 + 4\right)\left(X_2 - 1\right) - \cos\left(5X_1\right) + \sum_{k=1}^{20} X_k^2 \tag{30}$$

where $\boldsymbol{X} = \{X_1, \ldots, X_{20}\}$ is a vector of normal random variables, and each X_i has the mean of 1 and the standard deviation of 0.2. Then, the P_f is defined as

$$P_f = \Pr\{Y \geq u_{\mathrm{thr}}\} \tag{31}$$

where the threshold u_{thr} is set as 27.5. Obviously, the EEV Y_{EEV} is equal to the Y itself.

Fig. 5 shows the performance of the AK-PDEMi for Example 2, and a total of $N_{\text{loop}}=10$ outer and inner loops are needed. As shown in Fig. 5(a), the PIE curve consists of 10 descending branches, and the EEVs of new training samples are grossly greater than the u_{ROI}, that is, locating inside the ROI. As a result, a good accordance between the Kriging predictions $\hat{\mathcal{Y}}_{\text{RP}}$ and the true counterparts $\mathcal{Y}_{\text{RP}}$ is achieved in the ROI, see Fig. 5(b). Thanks to the failure-informed enrichment scheme in the outer loop, the assigned probabilities of the representative points in the ROI are reduced significantly; see Fig. 5(c). As the outer and inner loops proceed sequentially, the $p_{Y_{\text{EEV}}}(y)$ yielded by the AK-PDEMi is gradually consistent to the histogram of the crude MCS; see Fig. 5(d). As shown in Figs. 5(e) and 5(f), the $\hat{u}_{\text{ROI}}$ and the $\hat{P}_f$ converges to their reference values at the end of the AK-PDEMi.

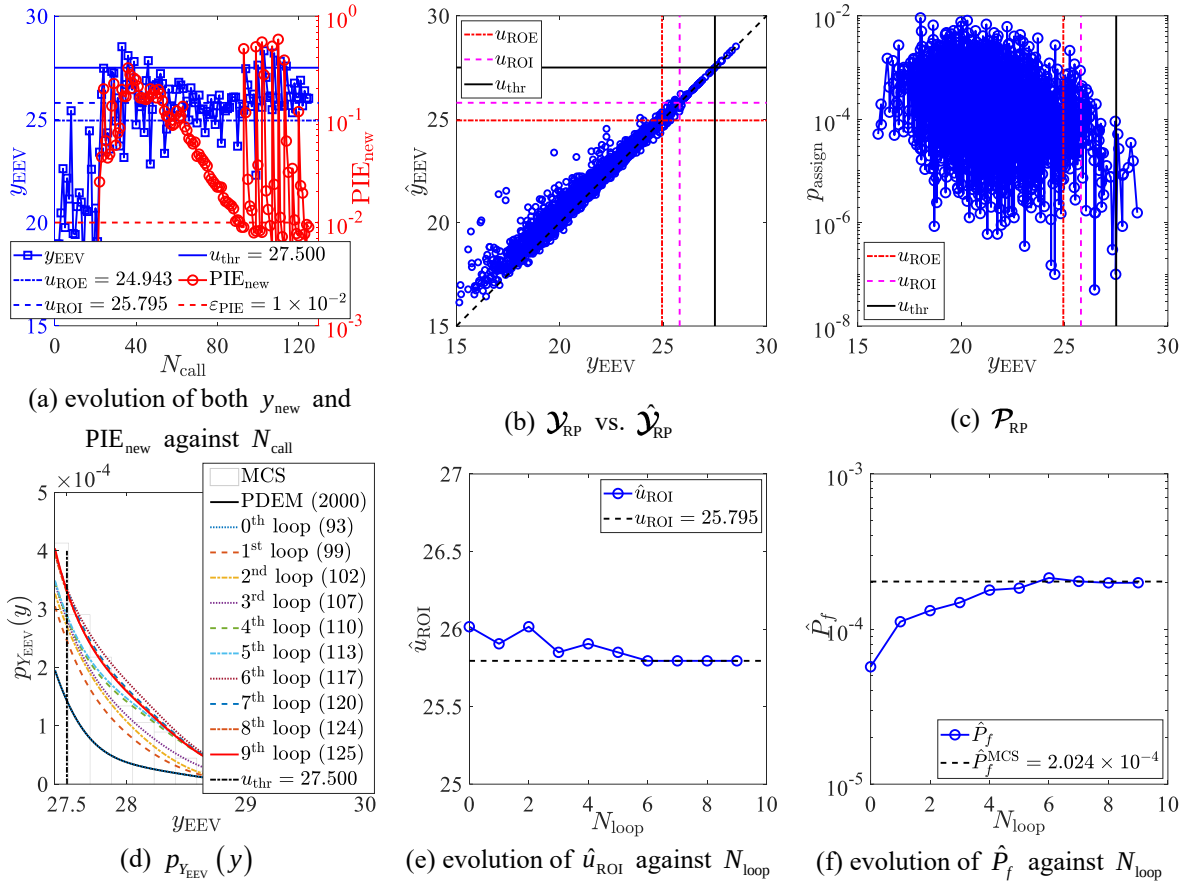

(a) evolution of both y_{new} and PIE_{new} against N_{call}

(b) $\mathcal{Y}_{\text{RP}}$ vs. $\hat{\mathcal{Y}}_{\text{RP}}$

(c) $\mathcal{P}_{\text{RP}}$

(d) $p_{Y_{\text{EEV}}}(y)$

(e) evolution of $\hat{u}_{\text{ROI}}$ against N_{loop}

(f) evolution of $\hat{P}_f$ against N_{loop}

Fig. 5 Performance of the proposed AK-PDEMi in Example 2

Table 2 lists the results of different reliability analysis algorithms for Example 2. The FORM still performs poorly. Both the IS and the SuS gain relatively fair estimates of failure probability, but their computational costs are too high. On the contrary, the AK-MCS, the APCK-IS and the APCK-SuS reduce remarkably the number of computational model evaluations, while gaining fair estimates of failure probability, especially in the APCK-SuS. In comparison with the AK-PDEM, the $\hat{P}_f$ provided by the AK-PDEMi is more consistent with the $\hat{P}_f^{\text{MCS}}$.

Table 2. Comparisons of different methods in Example 2

Method	N_{call}		$\hat{P}_f$ $(\times10^{-4})$		$\delta_{\hat{P}_f}$ (%)
	Median	$[q_{25}, q_{75}]$	Median	$[q_{25}, q_{75}]$	
MCS	5×10^7	-	2.024	-	-
FORM	816	-	0.465	-	77.04
IS	4816	[4816, 6816]	1.802	[1.754, 1.823]	10.95

SuS	7400	[7400, 7400]	1.998	[1.795, 2.335]	1.31
AK-MCS	>500	[>500, >500]	1.855	[1.770, 1.980]	8.35
APCK-IS	395.5	[337, 489]	1.863	[1.791, 1.969]	7.97
APCK-SuS	>500	[>500, >500]	2.020	[1.957, 2.058]	0.20
PDEM	2000	-	0.571	-	71.78
AK-PDEM	88.5	[88, 91]	0.571	[0.571, 0.572]	71.78
AK-PDEMi	126	[123, 133.5]	1.985	[1.979, 2.001]	1.92

Moreover, in order to testify the efficacy of the AK-PDEMi in the case of smaller failure probabilities, the threshold u_{thr} in Eq. (31) is reset as 28.7, and the reference value $\hat{P}_f^{\text{MCS}}$ provided by the crude MCS with 5×10^7 trials is equal to 2.171×10^{-5}. Then, Fig. 6 shows the performance of the AK-PDEMi, which involves $N_{\text{loop}}=10$ outer and inner loops. A good accordance between the $\hat{\mathcal{Y}}_{\text{RP}}$ and the $\mathcal{Y}_{\text{RP}}$ in the ROI is observed in Fig. 6(b). The magnitude of the assigned probabilities of representative points in the ROI is reduced in Fig. 6(c), owing to the failure-informed enrichment scheme. As both the outer and inner loops proceed, the $p_{Y_{\text{EEV}}}(y)$ provided by the AK-PDEMi gradually converges to the histogram of the crude MCS; see Fig. 6(d). Finally, Fig. 6(f) shows that the $\hat{P}_f$ in the last loop is equal to 2.296×10^{-5}, with the $\delta_{\hat{P}_f}$ being 5.76%. Hence, the AK-PDEMi still achieves relatively fair results in the failure probability level of 10^{-5}.

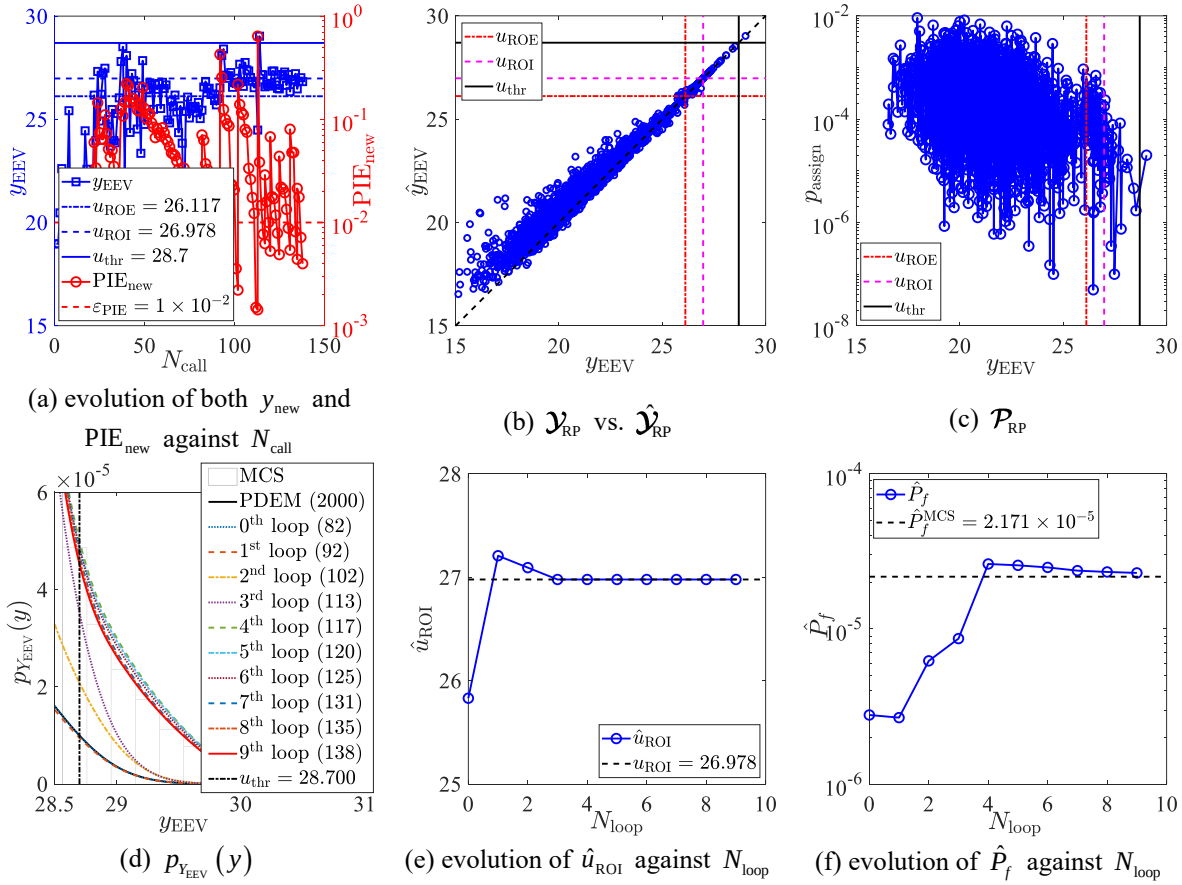

(a) evolution of both y_{new} and PIE$_{\text{new}}$ against N_{call} (b) $\mathcal{Y}_{\text{RP}}$ vs. $\hat{\mathcal{Y}}_{\text{RP}}$ (c) $\mathcal{P}_{\text{RP}}$

(d) $p_{Y_{\text{EEV}}}(y)$ (e) evolution of $\hat{u}_{\text{ROI}}$ against N_{loop} (f) evolution of $\hat{P}_f$ against N_{loop}

Fig. 6. Performance of the proposed AK-PDEMi in the case of smaller failure probability

When dealing with even smaller failure probabilities, e.g., $P_f=10^{-7}\sim10^{-9}$, the AK-PDEMi may become more challenging, and the reasons are stated as follows. Eq. (16) shows that the integral of the partial PDF $p_{Y_{\text{EEV}}}^{(j)}(y)$ over the whole domain is equal to the assigned probability $p_{\text{assign}}^{(j)}$. If the target failure probability P_f is

much smaller, the magnitude of the assigned probabilities of representative points in the ROI also needs to be decreased to a comparable level. To reduce the assigned probabilities to such a small level, a large number of representative points are needed to be enriched to the ROE. Accordingly, the number of training samples will be increased remarkably. Besides, as shown in Fig. 6(f), the outer-loop convergence criterion may give rise to the premature termination of the AK-PDEMi. Hence, a more appropriate convergence criterion for terminating the failure-informed enrichment scheme may be needed in the case of much smaller failure probabilities.

4.3 Seismic reliability analysis of a shear-frame structure

The third example addresses the seismic reliability analysis of a 10-story shear-frame structure, as sketched in Fig. 6(a). The lumped masses of each floor are valued as: $m_1 = 3.487$, $m_2 = 3.225$, $m_3 = 2.887$, $m_4 = 2.667$, $m_5 = \ldots = m_{10} = 2.558$ ($\times 10^5$ kg). The initial inter-story stiffnesses of each floor are considered as lognormal random variables, and their means and COVs are provided in Table 3. The height of each floor is taken as 3.7 m. The nonlinear inter-story hysteretic behavior is described by the extended Bouc-Wen model [34,35], and the 13 involved parameters are valued by: $\alpha_{\mathrm{BW}} = 0.04$, $A_{\mathrm{BW}} = 1$, $n_{\mathrm{BW}} = 1$, $\beta_{\mathrm{BW}} = 320$, $\gamma_{\mathrm{BW}} = 150$, $\delta_{\nu_{\mathrm{BW}}} = 2000$, $\delta_{\eta_{\mathrm{BW}}} = 2000$, $p_{\mathrm{BW}} = 1000$, $q_{\mathrm{BW}} = 0.25$, $\psi_{\mathrm{BW}} = 0.05$, $\delta_{\psi_{\mathrm{BW}}} = 5$, $\lambda_{\mathrm{BW}} = 0.5$, $\zeta_{s_{\mathrm{BW}}} = 0.99$. Then, a typical hysteretic curve of the first floor is shown in Fig. 6(b).

Table 3. Initial inter-story stiffnesses ($\times 10^8$ N/m)

Variables	k_1	k_2	k_3	k_4	k_5	k_6	k_7	k_8	k_9	k_{10}
Mean	1.962	1.875	1.758	1.754	1.662	1.662	1.662	1.662	1.662	1.662
COV	0.1	0.1	0.1	0.1	0.1	0.1	0.1	0.1	0.1	0.1

The input excitation takes the El-Centro ground motion (N-S component), of which the peak ground acceleration is scaled to 3.45 $\mathrm{m/s^2}$ (Fig. 6(c)). Rayleigh damping $\boldsymbol{C} = a\boldsymbol{M} + b\boldsymbol{K}$ is adopted, where $\boldsymbol{M}$ and $\boldsymbol{K}$ denotes the mass and initial stiffness matrices, respectively; then, the two coefficients, a and b, are taken as 0.2904 $\mathrm{s^{-1}}$ and 0.0066 s, respectively. Hence, a total of 10 random variables are involved in the dynamic system, i.e., $\boldsymbol{X} = \{k_1, k_2, \ldots, k_{10}\}$.

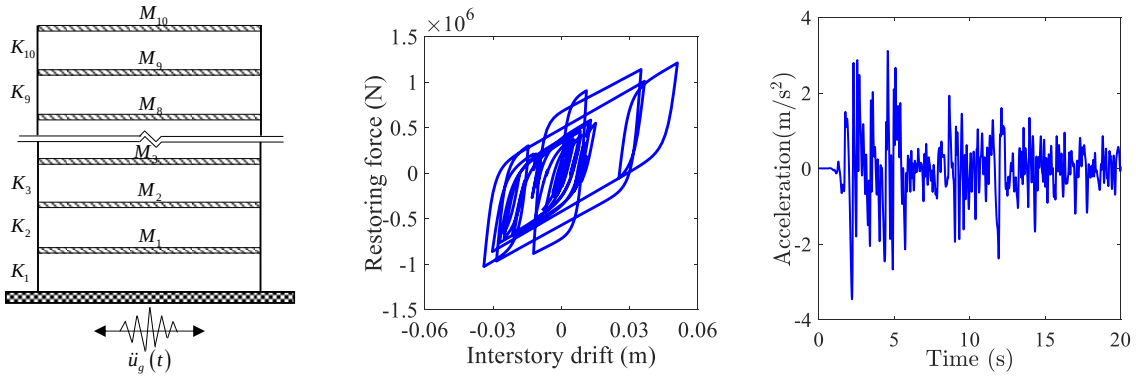

(a) geometric layout (b) hysteretic curve of first floor (c) the scaled El-Centro accelerogram

Fig. 7. Illustration of the shear-frame structure

The system reliability of this structure is of concern and the P_f is defined as

$$P_f = \Pr\left\{\bigcup_{j=1}^{10}\left(\exists t \in [0, 20\mathrm{s}], U_j(\boldsymbol{X}, t) \geq u_{\mathrm{thr}}\right)\right\} \tag{32}$$

where $U_j(\boldsymbol{X},t)$, j = 1, …, 10, denotes the inter-story drift of the j-th story; u_{thr} is the threshold and is assumed as 74 mm. Then, Eq. (32) is equivalent to $P_f = \Pr\{Y_{\text{EEV}} \geq u_{\text{thr}}\} = \int_{u_{\text{thr}}}^{+\infty} p_{Y_{\text{EEV}}}(y)dy$, with the Y_{EEV} defined as

$$Y_{\text{EEV}} = \max_{1\leq j\leq 10}\left(\max_{t\in[0,20\text{s}]}\left|U_j(\boldsymbol{X},t)\right|\right) \tag{33}$$

Fig. 8 presents the performance of the AK-PDEMi for Example 3, and a total of N_{loop} =11 outer and inner loops are involved. As shown in Fig. 8(a), there are 11 descending branches in the PIE curve and most of new training samples are located in the ROI. Consequently, the Kriging predictions $\hat{\mathcal{Y}}_{\text{RP}}$ are in a good accordance with the $\mathcal{Y}_{\text{RP}}$ in the ROI; see Fig. 8(b). Due to the enrichment of representative points in the ROE, the assigned probabilities of representative points in the ROI are smaller than those in other regions, as shown in Fig. 8(c). The convergence performance of the $p_{Y_{\text{EEV}}}(y)$ curves produced by the AK-PDEMi is shown in Fig. 8(d), and the $p_{Y_{\text{EEV}}}(y)$ finally achieves a good accordance with the histogram of the crude MCS. Both the $\hat{u}_{\text{ROI}}$ and the $\hat{P}_f$ converge to their reference values at the end of AK-PDEMi, see Figs. 8(e) and (f).

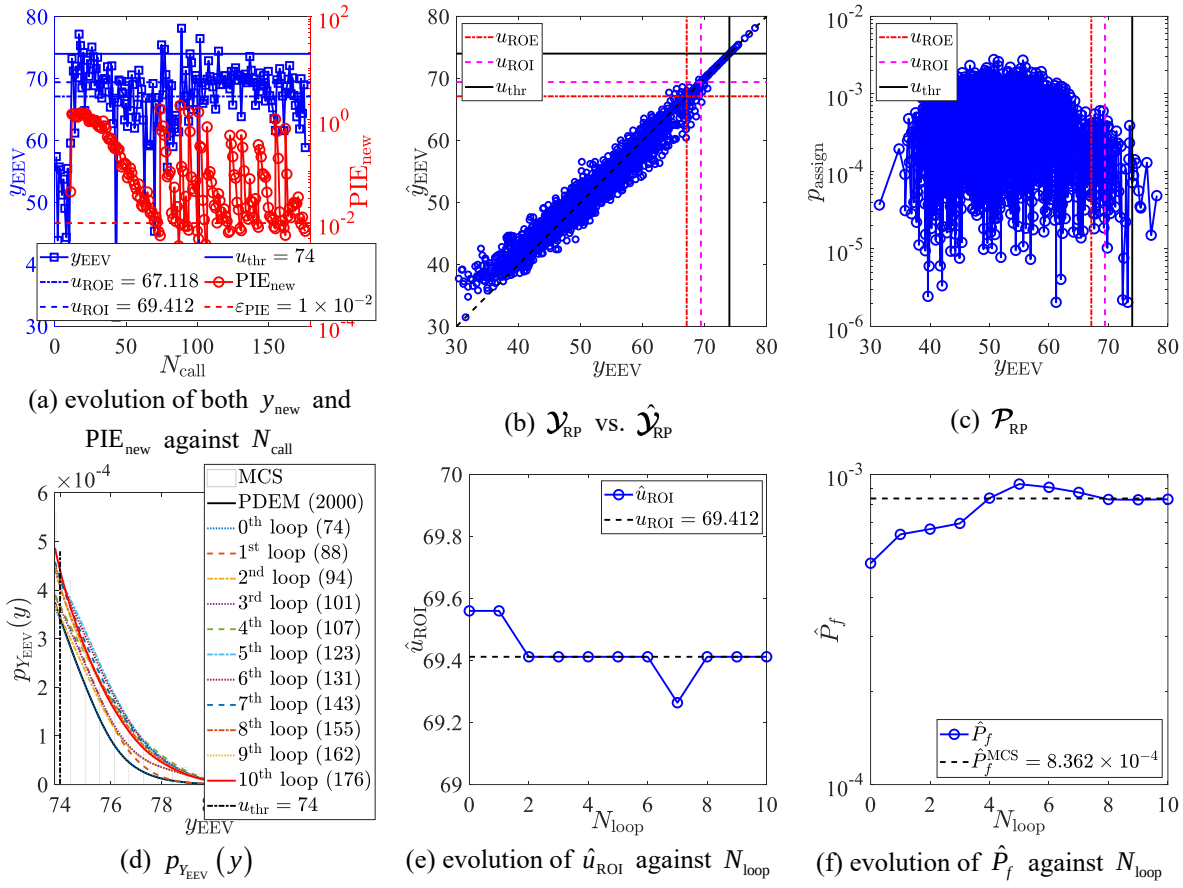

(a) evolution of both y_{new} and PIE_{new} against N_{call}

(b) $\mathcal{Y}_{\text{RP}}$ vs. $\hat{\mathcal{Y}}_{\text{RP}}$

(c) $\mathcal{P}_{\text{RP}}$

(d) $p_{Y_{\text{EEV}}}(y)$

(e) evolution of $\hat{u}_{\text{ROI}}$ against N_{loop}

(f) evolution of $\hat{P}_f$ against N_{loop}

Fig. 8. Performance of the AK-PDEMi for Example 3

Table 4 provides the results of different reliability analysis algorithms for Example 3. Both the IS and the SuS achieve good estimates of failure probability at the expense of extremely large number of deterministic structural analyses. The AK-MCS, the APCK-IS and the APCK-SuS provide inferior results in this example. In comparison with the existing AK-PDEM, the proposed AK-PDEMi enables to improve the accuracy of failure probability with fair efficiency.

Table 4. Comparisons of different reliability methods in Example 3

Method	N_{call}		$\hat{P}_f$ $(\times 10^{-4})$		$\delta_{\hat{P}_f}$ (%)
	Median	$[q_{25}, q_{75}]$	Median	$[q_{25}, q_{75}]$	
MCS	5×10^6	-	8.362	-	-
FORM	1574	-	52.031	-	519.05
IS	17574	[15574, 19574]	8.311	[8.137, 8.485]	1.11
SuS	7400	[5600, 7400]	8.732	[7.460, 11.150]	3.89
AK-MCS	>500	[>500, >500]	4.925	[4.580, 5.225]	41.10
APCK-IS	>500	[>500, >500]	4.734	[4.133, 5.071]	43.39
APCK-SuS	>500	[>500, >500]	4.516	[4.295, 4.997]	46.00
PDEM	2000	-	5.183	-	38.02
AK-PDEM	76	[71.5, 78]	5.183	[5.170, 5.172]	38.02
AK-PDEMi	174.5	[170.5, 183]	8.302	[8.293, 8.305]	0.72

5 Concluding remarks

An efficient reliability method called the AK-PDEMi was proposed. In the AK-PDEMi, a failure-informed enrichment scheme is devised to sequentially enrich the representative points with another new sets of representative points, and its convergence criterion is defined based on the stabilization of failure probability estimates. This scheme is featured by sequentially making fine partitions of the ROI, so as to reduce the PDEM-associated discretization error. Both the failure-informed enrichment scheme and the adaptive refinement of the Kriging are complementary and serve as the outer and inner loops of the AK-PDEMi, respectively. Then, the outer and inner loops proceed sequentially until both of their convergence criteria are satisfied. Comparisons are made between the AK-PDEMi and other conventional reliability analysis algorithms, including the FORM, the IS, the SuS, the AK-MCS, the APCK-IS, the APCK-SuS, the standard PDEM and the existing AK-PDEM. Some concluding remarks are given as follows.

(1) The existing AK-PDEM agrees well with the standard PDEM, but may yield unsatisfactory performance, due to the empirical setting of the sample size of representative points.

(2) In comparison with the existing AK-PDEM, the AK-PDEMi consists of two loops, i.e., the outer loop sequentially making fine partitions of the key sub-region in the ROI by enriching new representative points to the ROE, and the inner loop adaptively refining the Kriging accuracy in the ROI by placing training samples in such area. The two loops are complementary and enable to reduce both the PDEM-associated discretization error and the Kriging-incurred error.

(3) In comparison with other existing reliability methods, the AK-PDEMi has significant superiority in terms of both computational accuracy and efficiency.

It is admitted that how to further tackle with the case of much smaller failure probabilities using the AK-PDEMi still needs investigations, and a more pertinent convergence criterion for the outer loop of the AK-PDEMi is also needed to ensure the fair termination of the AK-PDEMi.

Acknowledgements

The supports of the National Natural Science Foundation of China (Grant No. 51878505), the Natural Science Foundation of Shanghai (Grant No. 21ZR1425500) and the Ministry of Science and Technology of PR China (Grant No. SLDRCE 19-B-26) are highly appreciated. The first author gratefully acknowledges the financial support from the China Scholarship Council (Grant No. 202006260201) for his study at the ETH Zurich.

Appendix A: GF discrepancy-based strategy

Consider a representative point set $\mathcal{X}_{\mathrm{RP}}=\left\{\boldsymbol{x}^{(1)},\ldots,\boldsymbol{x}^{(N_{\mathrm{RP}})}\right\}$ and its assigned probabilities $\mathcal{P}_{\mathrm{RP}}=\left\{p_{\mathrm{assign}}^{(1)},\ldots,p_{\mathrm{assign}}^{(N_{\mathrm{RP}})}\right\}$, the worst error raised by the PDEM satisfies the extended Koksma-Hlawka inequality [36]

$$\left|\int_{\Omega_{\boldsymbol{X}}} p_{VX}\left(v,\boldsymbol{x},\tau\right)d\boldsymbol{x}-\sum_{j=1}^{N_{\mathrm{RP}}}p_{V}^{(j)}\left(v,\tau\right)\right|\le\mathcal{O}\left(d\right)\cdot D_{\mathrm{GF}}\left(\mathcal{X}_{\mathrm{RP}}\right)\cdot\mathrm{TV}\left(\mathcal{M}\right) \tag{A1}$$

where $\mathcal{O}\left(d\right)$ denotes the same order of the magnitude of d, and d is the dimension of $\boldsymbol{X}$; $\mathrm{TV}\left(\mathcal{M}\right)$ is the total variation related to the irregularity of the computational function $\mathcal{M}$; $D_{\mathrm{GF}}\left(\mathcal{X}_{\mathrm{RP}}\right)$ is the GF-discrepancy of the point set $\mathcal{X}_{\mathrm{RP}}$ and is defined as

$$D_{\mathrm{GF}}\left(\mathcal{X}_{\mathrm{RP}}\right)=\max_{1\le k\le d}\left\{\sup_{-\infty\le x\le\infty}\left|F_{X_k}\left(x\right)-F_{X_k}^{\mathrm{E}}\left(x\right)\right|\right\} \tag{A2}$$

where $F_{X_k}\left(\cdot\right),k=1,\ldots,d,$ is the marginal CDF of the k-th variable X_k; $F_{X_k}^{\mathrm{E}}\left(\cdot\right)$ is the empirical marginal CDF of X_k, accounting for the effects of the assigned probabilities $\mathcal{P}_{\mathrm{RP}}$, that is,

$$F_{X_k}^{\mathrm{E}}\left(x\right)=\sum_{j=1}^{N_{\mathrm{RP}}}p_{\mathrm{assign}}^{(j)}\cdot I\left\{x_k^{(j)}\le x\right\} \tag{A3}$$

where $x_k^{(j)}$ is the k-th component of $\boldsymbol{x}^{(j)}\in\mathcal{X}_{\mathrm{RP}}$.

Eq. (A1) indicates that the point set with the minimal GF discrepancy is taken as the representative point set of the PDEM. To this end, a GF discrepancy-based point rearrangement strategy was developed in [30]. First, an initial point set $\mathcal{U}_0=\left\{\boldsymbol{u}^{(1)},\ldots,\boldsymbol{u}^{(N_{\mathrm{RP}})}\right\}$ of size N_{RP} is generated from the Sobol sequence in the unit hypercube; and the isoprobabilistic transformation is performed such that

$$\boldsymbol{x}^{(j)}=F_{\boldsymbol{X}}^{-1}\left(\boldsymbol{u}^{(j)}\right),j=1,\ldots,N_{\mathrm{RP}}. \tag{A4}$$

which converts the $\mathcal{U}_0$ to the initial point set $\mathcal{X}_0=\left\{\boldsymbol{x}^{(1)},\ldots,\boldsymbol{x}^{(N_{\mathrm{RP}})}\right\}$ in the physical space. The assigned probabilities $\mathcal{P}_{\mathrm{RP},0}$ of the $\mathcal{X}_0$ are numerically computed via Eq. (10).

Then, the rearrangement of point set is conducted based on both the $\mathcal{X}_0$ and the $\mathcal{P}_{\mathrm{RP},0}$ such that [30]

$$\breve{x}_k^{(l)}=F_k^{-1}\left(\sum_{j=1}^{N_{\mathrm{RP}}}p_{\mathrm{assign}}^{(j)}\cdot I\left\{x_k^{(j)}<x_k^{(l)}\right\}+\frac{1}{2}p_{\mathrm{assign}}^{(j)}\right),k=1,\ldots,d,l=1,\ldots,N_{\mathrm{RP}} \tag{A5}$$

so as to reduce the GF-discrepancy of the $\mathcal{X}_0$. The rearranged point set is denoted by $\mathcal{X}_{\mathrm{RP}}=\left\{\breve{\boldsymbol{x}}^{(1)},\ldots,\breve{\boldsymbol{x}}^{(N_{\mathrm{RP}})}\right\}$, and its assigned probabilities $\mathcal{P}_{\mathrm{RP}}$ are then recomputed by Eq. (10). In this regard, both the representative point set $\mathcal{X}_{\mathrm{RP}}$ and its assigned probabilities $\mathcal{P}_{\mathrm{RP}}$ are obtained for the PDEM.

Appendix B: Iterative determination of the boundary of ROI

Algorithm B1: Iterative determination of the u_{ROI}

1: **Input:** $\left\{P_f^{(1)},\ldots,P_f^{(N_{\mathrm{RP}})}\right\}$, $\mathcal{Y}_{\mathrm{RP}}=\left\{y_{\mathrm{EEV}}^{(1)},\ldots,y_{\mathrm{EEV}}^{(N_{\mathrm{RP}})}\right\}$ and the threshold u_{thr}.
2: **Initialization:**
3: The increment $u_{\mathrm{inc}}=u_{\mathrm{thr}}/100$; the initial $u_{\mathrm{ROI}}=u_{\mathrm{thr}}$.
4: **Iterative algorithm:** In step k = 1, 2, …,
5: If Eq. (19) is satisfied, then
6: Break.
7: Else
8: $u_{\mathrm{ROI}}=u_{\mathrm{ROI}}-u_{\mathrm{inc}}$, $k=k+1$.
9: End
10: **Return:** u_{ROI}.

Appendix C: Kriging model

The Kriging model $\hat{\mathcal{M}}^{\mathrm{K}}$ interprets the computational model $\mathcal{M}$ in Eq. (7) as a realization of Gaussian process such that [37]

$$\hat{y}_{\mathrm{EEV}}\approx\hat{\mathcal{M}}^{\mathrm{K}}(\boldsymbol{x})=\boldsymbol{\beta}^{\mathrm{T}}\boldsymbol{f}(\boldsymbol{x})+\sigma^2 Z(\boldsymbol{x}) \tag{C1}$$

where $\boldsymbol{\beta}^{\mathrm{T}}\boldsymbol{f}(\boldsymbol{x})$ is the trend of Kriging model and the ordinary Kriging is utilized, that is, $\boldsymbol{f}(\boldsymbol{x})=1$ and β is unknown; σ^2 is the process variance; $Z(\boldsymbol{x})$ is a zero-mean, unit-variance Gaussian process represented by a correlation function $R(\boldsymbol{x},\boldsymbol{x}')$. Here, the Matern-3/2 correlation function [37] is adopted such that

$$R(\boldsymbol{x},\boldsymbol{x}';\boldsymbol{\theta})=\left(1+\sqrt{3}\cdot\sqrt{\sum_{k=1}^{d}\left(\frac{x_k-x_k'}{\theta_k}\right)^2}\right)\exp\left(-\sqrt{3}\cdot\sqrt{\sum_{k=1}^{d}\left(\frac{x_k-x_k'}{\theta_k}\right)^2}\right) \tag{C2}$$

where $\boldsymbol{\theta}=\{\theta_k>0\}_{k=1}^{d}$ denotes the correlation parameters.

Consider a training dataset $\mathcal{D}=\{\mathcal{X},\mathcal{Y}\}$ consisting of the experimental design $\mathcal{X}=\left\{\boldsymbol{x}^{(1)},\ldots,\boldsymbol{x}^{(N)}\right\}$ and the corresponding computational model evaluations $\mathcal{Y}=\left\{y_{\mathrm{EEV}}^{(1)},\ldots,y_{\mathrm{EEV}}^{(N)}\right\}$, both the β and the σ^2 are estimated by

$$\hat{\beta}(\boldsymbol{\theta})=\left(\mathbf{1}^{\mathrm{T}}\boldsymbol{R}^{-1}\mathbf{1}\right)^{-1}\mathbf{1}^{\mathrm{T}}\boldsymbol{R}^{-1}\mathcal{Y} \tag{C3}$$

$$\hat{\sigma}^2(\boldsymbol{\theta})=\frac{1}{N}\left(\mathcal{Y}-\mathbf{1}^{\mathrm{T}}\hat{\beta}\right)^{\mathrm{T}}\boldsymbol{R}^{-1}\left(\mathcal{Y}-\mathbf{1}^{\mathrm{T}}\hat{\beta}\right) \tag{C4}$$

where $\mathbf{1}$ is vector filled with 1 of length N; $\boldsymbol{R}$ is the correlation matrix with elements $R^{(i,j)}=R\left(\boldsymbol{x}^{(i)},\boldsymbol{x}^{(j)};\boldsymbol{\theta}\right)$, i, j = 1, …, N. Eqs. (C3) and (C4) show that both the $\hat{\beta}$ and the $\hat{\sigma}^2$ depend on the $\boldsymbol{\theta}$ through the matrix $\boldsymbol{R}$. Hence, the $\boldsymbol{\theta}$ needs to be firstly calibrated by the maximum likelihood method [37], that is,

$$\hat{\boldsymbol{\theta}}=\arg\min_{\boldsymbol{\theta}}\left(\hat{\sigma}^2(\boldsymbol{\theta})\left(\det\left(\boldsymbol{R}(\boldsymbol{\theta})\right)\right)^{\frac{1}{N}}\right) \tag{C5}$$

Finally, the Kriging predictor at an unknown point $\boldsymbol{x}$ follows normal distribution, i.e., $\hat{y}_{\mathrm{EEV}}\sim\mathcal{N}\left(\mu_{\hat{y}}(\boldsymbol{x}),\sigma_{\hat{y}}^2(\boldsymbol{x})\right)$, with the prediction mean and variance given by [37]

$$\mu_{\hat{y}}(\boldsymbol{x})=\hat{\beta}+\boldsymbol{r}(\boldsymbol{x})^{\mathrm{T}}\boldsymbol{R}^{-1}\left(\mathcal{Y}-\hat{\beta}\mathbf{1}\right) \tag{C6}$$

$$\sigma_{\hat{y}}^2(\boldsymbol{x})=\hat{\sigma}^2\left(1-\boldsymbol{r}(\boldsymbol{x})^{\mathrm{T}}\boldsymbol{R}^{-1}\boldsymbol{r}(\boldsymbol{x})+u(\boldsymbol{x})^{\mathrm{T}}\left(\mathbf{1}^{\mathrm{T}}\boldsymbol{R}^{-1}\mathbf{1}\right)^{-1}u(\boldsymbol{x})\right) \tag{C7}$$

where $\boldsymbol{r}(\boldsymbol{x})=\left[R\left(\boldsymbol{x},\boldsymbol{x}^{(1)}\right),\ldots,R\left(\boldsymbol{x},\boldsymbol{x}^{(N)}\right)\right]^{\mathrm{T}}$, and $u(\boldsymbol{x})=\mathbf{1}^{\mathrm{T}}\boldsymbol{R}^{-1}\boldsymbol{r}(\boldsymbol{x})-1$. The UQLab software [38] is used to calibrate the Kriging model.

References

[1] Li J, Chen J. *Stochastic Dynamics of Structures*: John Wiley and Sons; 2010.
[2] Zhou T, Peng Y, Li J. An efficient reliability method combining adaptive global metamodel and probability density evolution method. *Mech Syst Signal Process*. 2019;131:592-616.
[3] Zhao YG, Ono T. A general procedure for first/second-order reliability method (FORM/SORM). *Struct Saf*. 1999;21:95-112.
[4] Der Kiureghian A, Dakessian T. Multiple design points in first and second-order reliability. *Struct Saf*. 1998;20:37-49.
[5] Rubinstein RY, Kroese DP. *Simulation and the Monte Carlo Method*: John Wiley & Sons; 2016.
[6] Tabandeh A, Jia G, Gardoni P. A review and assessment of importance sampling methods for reliability analysis. *Struct Saf*. 2022;97, 102216.
[7] Au SK, Wang Y. *Engineering Risk Assessment with Subset Simulation*: Wiley Blackwell; 2014.
[8] Zhao Y-G, Lu Z-H. *Structural Reliability: Approaches from Perspectives of Statistical Moments*: John Wiley & Sons; 2021.
[9] Li J. A PDEM-based perspective to engineering reliability: From structures to lifeline networks. *Front Struct Civ Eng*. 2020;14:1056-65.
[10] Zhou T, Peng Y. Adaptive Bayesian quadrature based statistical moments estimation for structural reliability analysis. *Reliab Eng Syst Saf*. 2020;198, 106902.
[11] Li J, Chen J. The principle of preservation of probability and the generalized density evolution equation. *Struct Saf*. 2008;30:65-77.
[12] Teixeira R, Nogal M, O'Connor A. Adaptive approaches in metamodel-based reliability analysis: A review. *Struct Saf*. 2021;89, 102019.
[13] Moustapha M, Marelli S, Sudret B. Active learning for structural reliability: Survey, general framework and benchmark. *Struct Saf*. 2022; 96, 102174.
[14] Echard B, Gayton N, Lemaire M. AK-MCS: An active learning reliability method combining Kriging and Monte Carlo Simulation. *Struct Saf*. 2011;33:145-54.
[15] Marelli S, Sudret B. An active-learning algorithm that combines sparse polynomial chaos expansions and bootstrap for structural reliability analysis. *Struct Saf*. 2018;75:67-74.
[16] Moustapha M, Bourinet JM, Guillaume B, Sudret B. Comparative Study of Kriging and Support Vector Regression for Structural Engineering Applications. *ASCE-ASME J Risk Uncertain Eng Syst Part A Civ Eng. 2018;4*.
[17] Schöbi R, Sudret B. Structural reliability analysis for p-boxes using multi-level meta-models. *Probab Eng Mech*. 2017;48:27-38.
[18] Yi J, Wu F, Zhou Q, Cheng Y, Ling H, Liu J. An active-learning method based on multi-fidelity Kriging model for structural reliability analysis. *Struct Mutltidiscip Opt*. 2021;63:173-95.
[19] Zhang J, Xiao M, Gao L. An active learning reliability method combining Kriging constructed with exploration and exploitation of failure region and subset simulation. *Reliability Engineering & System Safety*. 2019;188:90-102.
[20] Xiao N-C, Zhan H, Yuan K. A new reliability method for small failure probability problems by combining the adaptive importance sampling and surrogate models. *Computer Methods in Applied Mechanics and Engineering*. 2020;372:113336.
[21] Zhou T, Peng Y. A new active-learning function for adaptive Polynomial-Chaos Kriging probability density evolution method. *Appl Math Model.* 2022; 106:86-99.
[22] Zhou T, Peng Y. Reliability analysis using adaptive Polynomial-Chaos Kriging and probability density evolution method. *Reliab Eng Syst Saf*. 2022; 220:108283.
[23] Bichon BJ, Eldred MS, Swiler LP, Mahadevan S, McFarland JM. Efficient global reliability analysis for nonlinear implicit performance functions. *AIAA J*. 2008;46:2459-68.
[24] Moustapha M, Sudret B. Surrogate-assisted reliability-based design optimization: a survey and a unified modular framework. *Struct Mutltidiscip Opt*. 2019;60:2157-76.
[25] Schöbi R, Sudret B, Marelli S. Rare Event Estimation Using Polynomial-Chaos Kriging. *ASCE-ASME J Risk Uncertain Eng Syst Part A Civ Eng*. 2017;3.
[26] Basudhar A, Missoum S. An improved adaptive sampling scheme for the construction of explicit boundaries. *Struct Mutltidiscip Opt*. 2010;42:517-29.
[27] Ling C, Lu Z, Feng K, Zhang X. A coupled subset simulation and active learning kriging reliability analysis method for rare failure events. *Struct Mutltidiscip Opt*. 2019;60:2325-41.
[28] Crandall SH. First-crossing probabilities of the linear oscillator. *J Sound Vib*. 1970;12:285-99.
[29] Li J, Chen J, Fan W. The equivalent extreme-value event and evaluation of the structural system reliability. *Struct Saf*. 2007;29:112-31.
[30] Chen J, Yang J, Li J. A GF-discrepancy for point selection in stochastic seismic response analysis of structures with uncertain parameters. *Struct Saf*. 2016;59:20-31.
[31] Aurenhammer F. Voronoi diagrams—a survey of a fundamental geometric data structure. *ACM Comput Surv*. 1991;23:345-405.
[32] Park JS. Optimal Latin-hypercube designs for computer experiments. *J Stat Plann Inference*. 1994;39:95-111.
[33] Li M, Wang Z. Deep learning for high-dimensional reliability analysis. *Mech Syst Signal Process*. 2020;139, 106399.

[34] Ma F, Zhang H, Bockstedte A, Foliente GC, Paevere P. Parameter analysis of the differential model of hysteresis. *J Appl Mech Trans ASME*. 2004;71:342-9.
[35] Li J, Peng Y, Chen J. Nonlinear stochastic optimal control strategy of hysteretic structures. *Struct Eng Mech*. 2011;38:39-63.
[36] Chen J, Yang J, Jensen H. Structural optimization considering dynamic reliability constraints via probability density evolution method and change of probability measure. *Struct Mutltidiscip Opt*. 2020;62:2499-516.
[37] Lataniotis C, Marelli S, Sudret B. The Gaussian Process Modeling Module in UQLab. *Journal of Soft Computing in Civil Engineering*. 2018;2:91-116.
[38] Marelli S, Sudret B. UQLab: A framework for uncertainty quantification in Matlab. *Proceeding of 2nd International Coference on Vulnerability, Risk Analysis and Management* 2014.